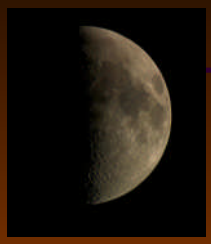

SELENOLOGY TODAY

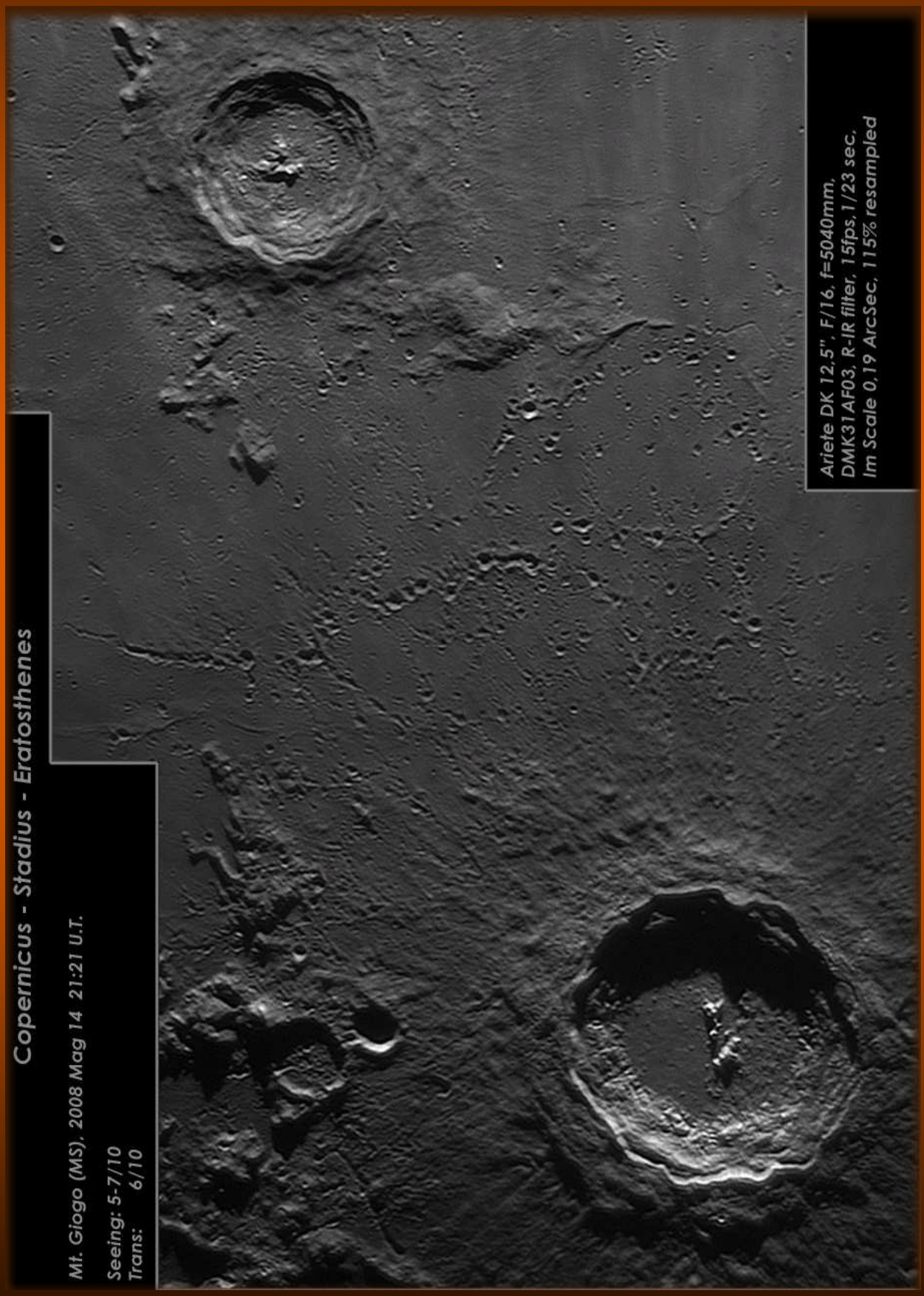

SELENOLOGY TODAY #11 October 2008

Selenology Today is devoted to the publication of contributions in the field of lunar studies.

Manuscripts reporting the results of new research concerning the astronomy, geology, physics, chemistry and other scientific aspects of Earth's Moon are welcome.

Selenology Today publishes papers devoted exclusively to the Moon.

Reviews, historical papers and manuscripts describing observing or spacecraft instrumentation are considered.

The Selenology Today

Editorial Office

selenology_today@christian-woehler.de

Cover
Raffaele Barzacchi
May 14 2008
21:21 UT

SELENOLOGY TODAY #11
October 2008

Selenology Today website
http://digilander.libero.it/glrgroup/

A Study about two domes near craters C. Herschel and Archytas, and an effusive dome in Mare Frigoris

By Raffaello Lena, Jim Phillips, Maria Teresa Bregante, Stefan Lammel and George Tarsoudis

Geologic Lunar Research (GLR) group

Abstract

In this study we examine three lunar domes located near the crater C. Herschel and Archytas, in Mare Frigoris. The diameters of the domes Archytas 1 and 2 are determined to 33.0 ± 1 km and 11.0 ± 0.4 km. Their heights amount to 70 ±120 m and 265 ± 30 m, resulting in flank slopes of 0.25° and 2.7°. The edifice volumes correspond to 22.4 and 12.6 km³. The dome Archytas 1 belongs to class In3 in the GLR classification scheme of intrusive domes while Archytas 2 belongs to class B1 of the GLR classification scheme of effusive domes. Archytas 1 is a large dome interpreted to be an intrusive structure due to the presence of a short straight rille and a fault traversing the surface, suggesting that its uplift resulted from the rise of magma that did not erupt onto the surface, producing a vertical rupture of the surface. It is the first lunar dome having a concentric crater on the summit.

Based on rheologic modelling we obtained for Archytas 2 dome effusion rate of 119 m^3 s^{-1}, magma viscosity of 4.4 x 10^6 and duration of the effusion process of 3.4 years. Furthermore, we have derived a magma rise speed of 4.4 x 10^{-6} m s^{-1} through a dike 170 km long and 114 m wide. In this study we have examined another dome located near the crater C. Herschel (CH1), which has a diameter of 16.8 ± 0.4 km, height of 64 ± 10 m , resulting in flank slope of 0.44°. The dome CH1 has a rille which cannot be unambiguously attributed to formation by tensional stress or flowing of lava. If it was assumed to be of intrusive origin, the dome C. Herschel 1 could be assigned to class In2. Regarding it as an effusive dome would imply to assign it to the effusive class C1.

1.Introduction

The Mare Basins were formed by large impacts. These impacts formed large cavities which collapsed. These collapses led to large-scale fracturing in the crust. The fractures are thought to be the conduits along which the basaltic magmas ascended to the surface. Lunar domes have formed as effusive shield-like volcanoes or as laccoliths, if the magma remained subsurface (Head and Gifford, 1980). The summit pit is an indication of the volcanic origin of these structures but it is not always present. Domes without a summit pit could still be volcanic in origin, but appear to have covered their central vent with lava (plug domes). Another possibility is that

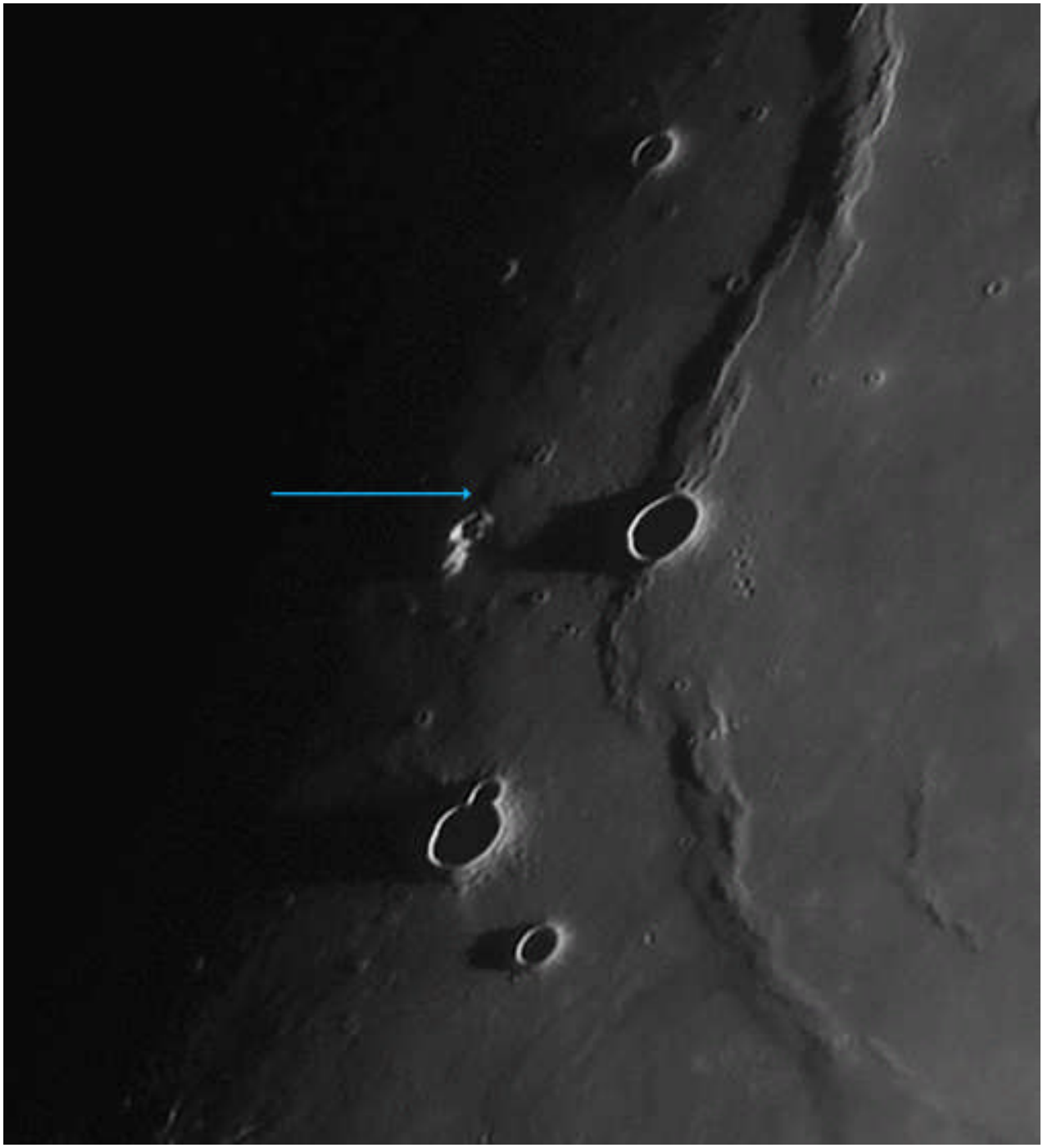

Fig. 1

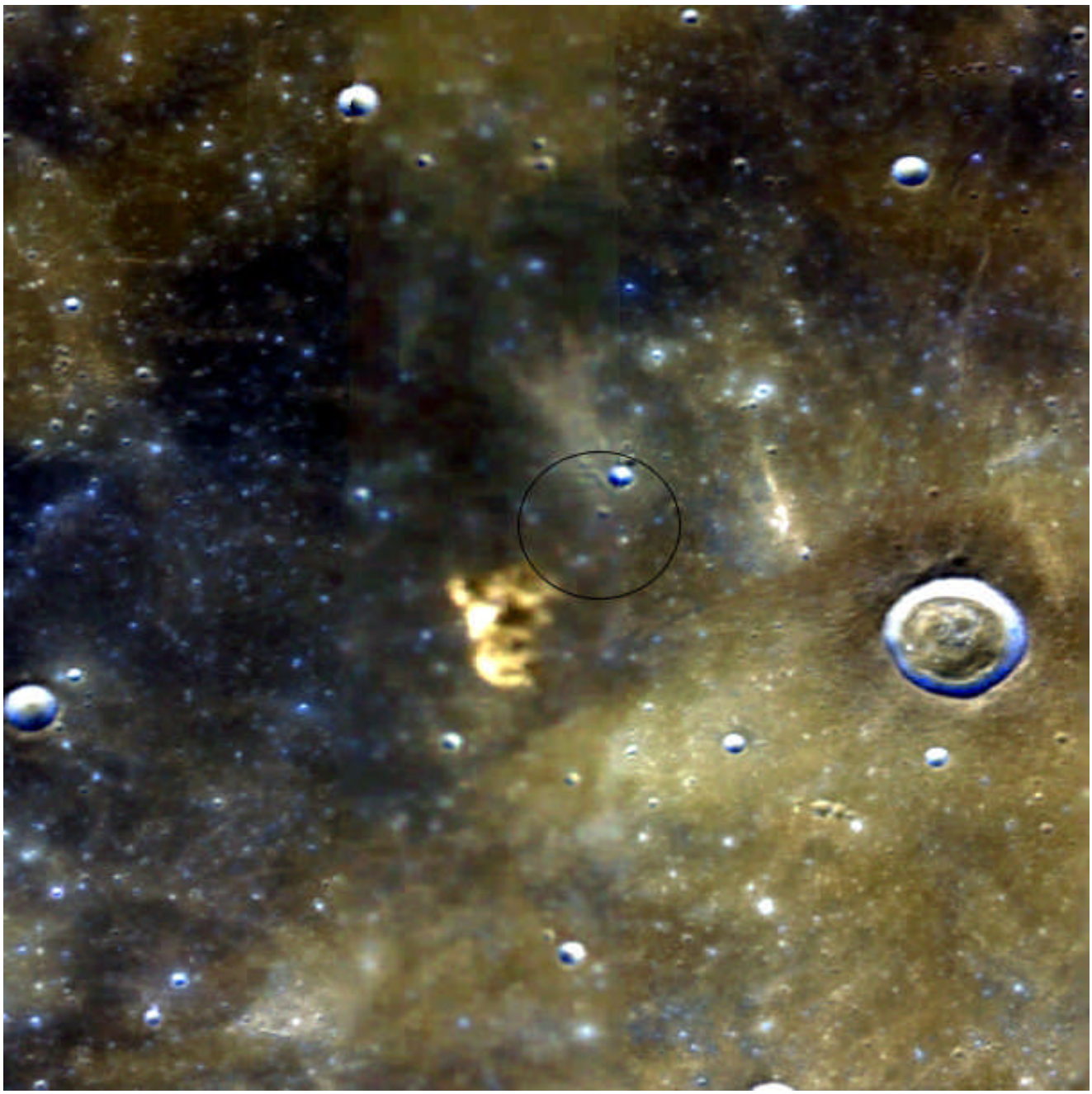

Fig. 2a

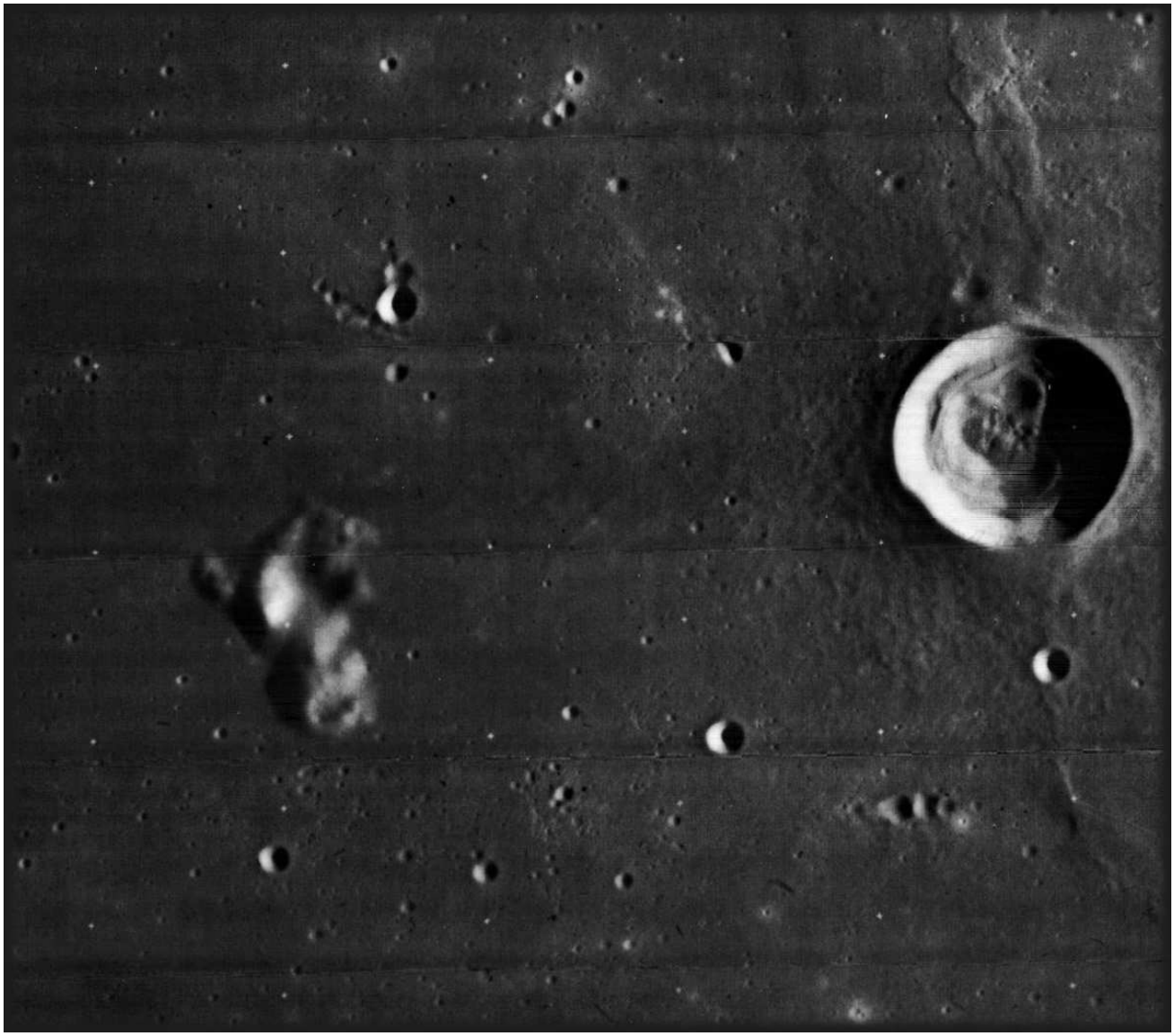

Fig. 2b

these domes represent intrusion of lava: the magma accumulated within the lunar crust, slowly increasing in pressure and causing the crustal rock above it to bow up-ward. The profile of domes that are flat suggests that there was no gradual inclination at the vent (the rising lava did not build up the dome in a series of flows) but a subsurface intrusion of magma (intrusive origin). Due to their low profile, Lunar Orbiter and Clementine images do not tend to show them very well, due to the typically high solar angle on such images. Hence, as part of our program of observations and cataloguing of lunar domes, we have used high resolution telescopic CCD images carried out under oblique illumination conditions. In this article we report measurement and include CCD images of two previously unlisted lunar domes, located at latitude 34.76°N and longitude 32.57°W (near crater C. Herschel) and latitude 56.52° N and 2.71° W (in Mare Frigoris). Moreover we examine another lunar dome in Mare Frigoris, possibly of intrusive origin, situated at 55.71°N and longitude 0.71°E.

2. Method and measurement

For each of the observations, the local solar altitude and the Sun's selenographic colongitude were calculated using the LTVT software package by Mosher and Bondo (2006) which requires a calibration of the images by identifying the precise selenographic coordinates of some landmarks on the image. This calibration was performed based on the UCLN 1994 list of control points. All images are oriented with north up and west (IAU) to the left.

Further morphometric data were obtained by a photoclinometric analysis (Horn, 1989; Carlotto, 1996; cf. also Wöhler et al., 2006; Lena et al., 2006 and references therein). We furthermore determined a UVVIS five-band spectrum of the dome based on Clementine imagery at the wavelengths of 415, 750, 900, 950, and 1000 nm. The sample area was 2x2 km^2. The reflectance values were derived relying on the calibrated and normalised Clementine UVVIS reflectance data as provided by Eliason et al. (1999). The extracted Clementine UVVIS data were examined in terms of 750 nm reflectance (albedo) and the R_{415}/R_{750} and R_{950}/R_{750} colour ratios. Albedo at 750 nm is an indicator of variations in soil composition, maturity, particle size, and viewing geometry.

The R_{415}/R_{750} colour ratio essentially is a measure for the TiO_2 content of mature basaltic soils, where high R_{415}/R_{750} ratios correspond to high TiO_2 content and vice versa (Charette et al., 1974). However, for many lunar regions the relation between R_{415}/R_{750} ratio and TiO_2 content displays a significant scatter (Gillis and Lucey, 2005). The R_{950}/R_{750} colour ratio is related to the strength of the mafic absorption band, representing a measure for the FeO content of the soil, and is also sensitive to the optical maturity of mare and highland materials (Lucey et al. 1998).

3. Region around C. Herschel. General description

Mare Imbrium sits in the Imbrium basin. The basin material is of the Lower Imbrian epoch, with the mare material being of the Upper Imbrian and Eratosthenian epochs (Wilhelms,1987). The mare is lined with mountain ranges to the south. The Alpes are part of the 1200 km diameter basin defining ring of Imbrium as also the Montes Carpatus in the south, the Apennines in the southeast, and the Montes Caucasus to the east. The Montes Caucasus and Alpes consist of rugged massifs that make up the rim crest of the Imbrium basin. The knobby Alpes formation, a unit with wide distribution around the Imbrium basin (Spudis, 1988; Spudis, 1993; Wilhelms,1987; Whitford-Stark, 1990) is found along the backslope of the basin rim crest in the north and east of the basin.

In the western segment of the basin exterior, hummocky to radially lineated Fra Mauro material makes up the backslope deposits (Spudis, 1988). Basalts of Mare Frigoris cover Imbrium basin deposits north of the basin rim at radial distances of 300-700 km from the rim crest. Mare Frigoris has complex stratigraphy with different basalt units (Spudis et al,1999). Most of the Mare is formed of low Titanium basalts (Whitford-Stark, 1990). On the basis of multispectral data derived from Celementine, Spudis et al. (1999) describe that Imbrium basin ejecta is broadly highland basaltic in composition, although specific areas are significantly anorthositic. Spudis et al (1999) examine the deposits of Imbrium basin suggesting that KREEP is abundant in the region, although its specific distribution appears to be not directly related to the distribution of Imbrium basin deposits. Moreover the distribution of KREEP, tracked by Th content, is not directly correlated with Imbrium basin ejecta, but has had a complex, multiphase history involving both impact and volcanic process (Spudis, 1993). Different lithological units, included in USGS lunar geologic map I-602, are apparent in the western part of Mare Imbrium, characterized by long wrinkle ridges and basalts of Imbrian age, mapped as 3 distinct units, Im1 through Im3, and described as flat, smooth material of mare areas (Schaber, 1969). We have studied a dome, located in the western part of Mare Imbrium, near a small lunar crater named C.Herschel, a circular bowl shaped formation. The crater lies on a wrinkle-ridge of the lunar mare named Dorsum Heim. No lunar domes located near Dorsum Heim and crater C. Herschel are reported in the USGS I-602, in ALPO catalogue and in the revised list of lunar domes (Kapral and Garfinkle, 2005). In the revised list is reported a dome of 3 km in diameter located at 31.76° W and 37.40° N, nearly 95 km to the north. It corresponds to a small crater of same dimension detectable in the image shown in Fig.1, just located to the east of crater C. Herschel C.

3.1 Telescopic CCD images, morphometric and spectral properties of the dome near C. Herschel

A shallow dome has been detected near

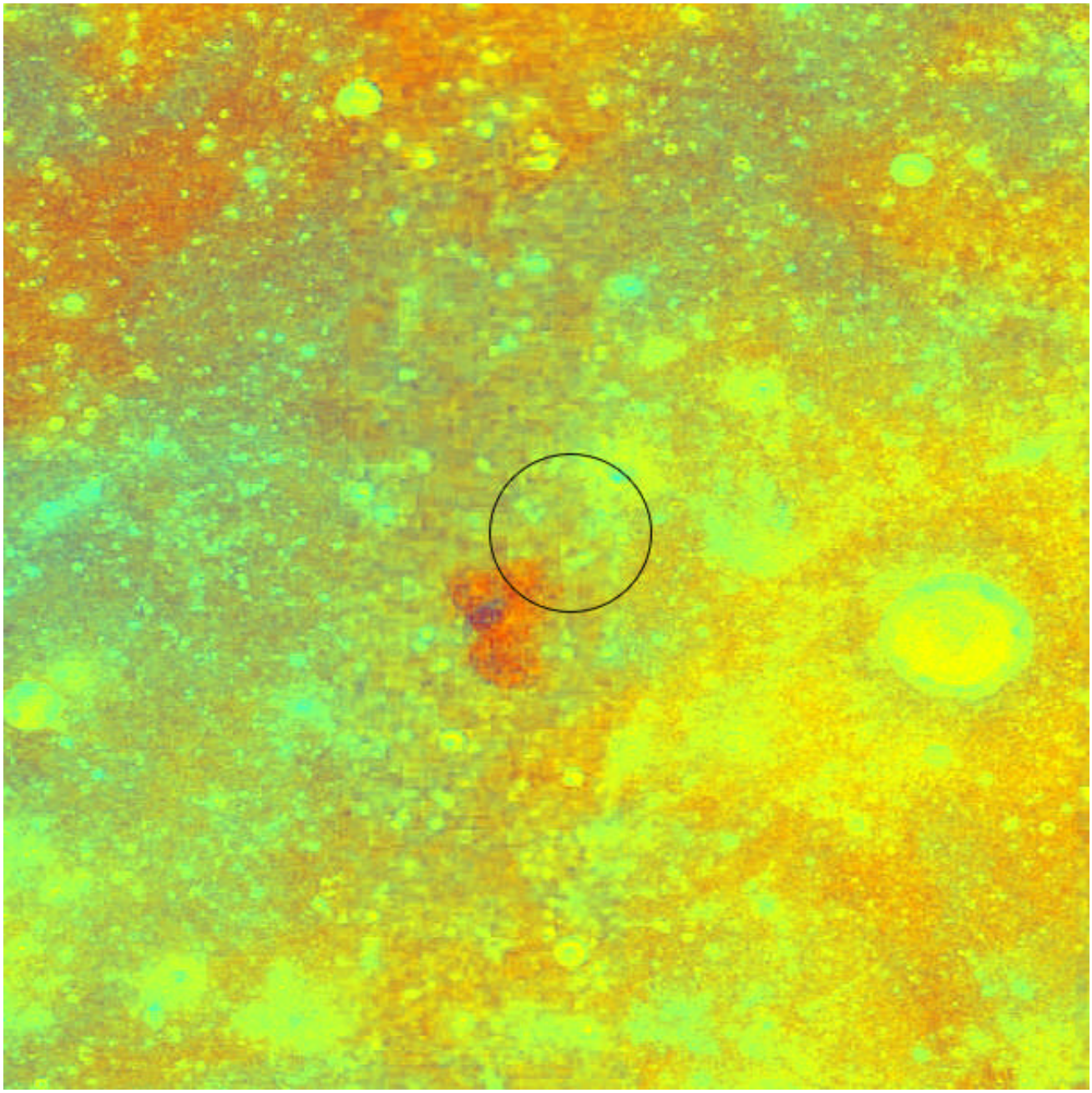

Fig. 3

the crater C. Herschel, located at 32.57° W and 34.76° N. According to our preceding studies we name the dome as C. Herschel 1 (CH 1).

The dome was detected in images taken by S. Lammel on February 16, 2008 at 21:22 UT using a 250 mm Newtonian telescope and a Lumenera Infinity 2-1M camera (Fig. 1). The dome diameter amounts to 16.8 ± 0.40 km. A very small dot is visible on the summit of CH1 in Fig. 1, possible indicating an effusive vent.

The effective height of the dome was obtained by determining elevation differences between the summit of the dome and its surroundings. This leads to a dome height of 64 ± 10 m, yielding an average flank slope of 0.44° ± 0.10°. We assumed a typical form factor of f = 1/2, which yields an estimated volume of V = 7.1 km³ based on the dome diameter D and height h given in Table 1.

The height of the dome was also computed from Figure 1 using the shadow length method according to the relation

$$h = l \tan \alpha \qquad (1)$$

where l is the shadow length, corrected for foreshortening and measured in km, and tan α the tangent of the solar altitude. A height of 62 ± 10 m was obtained, resulting in an average slope of 0.43° ± 0.10°.

Fig. 2a displays Clementine imagery, where an impact crater on the dome summit and its bright ejecta are recognisable. As visible in Fig. 2a, a slightly curved rille is located at the northern rim of the dome surface. This rille cannot be unambiguously attributed to formation by tensional stress or flowing of lava. In Fig. 2b, Orbiter imagery LO IV-139-H1, we have not identified any feature that resembles a vent, just some curved rilles that look like lava channels. Fig.3 shows the Clementine colour ratio, where fresh material due to impacts is recognisable.

The Clementine UVVIS spectral data of the dome CH1 reveal a 750 nm reflectance of R_{750} = 0.10513, a moderate value for the UV/VIS colour ratio of R_{415}/R_{750} = 0.59571, indicating a moderate TiO_2 content, and a strong mafic absorption with R_{950}/R_{750} = 1.00018, likely due to the fresh material excavated by the impact that formed the small crater on the top of the dome and by impacts of nearby craters. According to Schaber (1969) this examined region is composed of ray material (cf. USGS lunar geologic map I-602).

4. Mare Frigoris and region around Archytas. General description

Mare Frigoris is located just north of Mare Imbrium, and stretches east to north of Mare Serenitatis. Basalts in mare Frigoris are particular in that they occur in an area that is not clearly related to any unambiguously accepted impact structure. Mare Frigoris may be part of the large and very old Procellarum basin, but the existence of this basin is still disputed. The basin material surrounding the mare is of the Lower Imbrian epoch, while the eastern

mare material is of the Upper Imbrian epoch and the western mare material is of the Eratoshenian epoch (Lucchitta, 1978). Lucchita (1978) suggested that the concentration of Erstosthenian and Imbrian eruptions in Mare Frigoris, Imbrium, and Oceanus Procellarum is due to a thin lithosphere beneath the putative Procellarum basin.

The basalt fill within Mare Frigoris is thick (greater than 400 m) and was emplaced in at least three major episodes within topographic lows overlying a thick lunar lithosphere (Whitford-Stark, 1983 and references therein). The oldest identifiable unit is dominated by titanium-poor lavas and was succeeded by basalts of intermediate and titanium-rich composition. The lavas appear to have been emplaced largely by flood-style eruptions. Whitford-Stark (1983) suggested that the topographic low of western Frigoris was probably created by the collapse of highland blocks into the Imbrium impact cavity. The line of separation may have been an Imbrium ring fracture or a ring fracture of the older Procellarum basin. Parts of Frigoris have been mapped by Ulrich (1969), Lucchitta (1972), and M'Gonigle and Schleicher (1972), and a geologic map of the entire mare has been made by Lucchitta (1978). The volcanic tectonic evolution of Mare Frigoris was extensively examined by Whitford-Stark (1990). He provided a geologic map of the mare basalt units where red units indicate titanium-poor basalts and blue units, titanium-rich. Additionally the western basalts are correlated with the Sharp formation of Oceanus Procellarum and the reddish basalts with the Telemann formation of Procellarum (Whitford-Stark and Head, 1980).

Multispectral imagery only provide compositional data relating to the upper soil layer rather than the bedrock since the Mare Frigoris is extensively covered by rays from highland craters and from large craters within the mare, e.g. Harpalus and Aristoteles (cfr. Whitford-Stark, 1990 and references therein). The extent to which these spectra are representative of the underlying basalt is dependent upon the amount of highland material mixed with the locally derived soil. The geologic settings, along the eruption styles in Mare Frigoris are extensively examined by Whitford-Stark (1990).

Furthermore in Mare Frigoris a concentric crater, Archytas G, is situated. Concentric crater are small crater containing an inner ring about 1/2 the diameter of the main crater. Wood (1978) has examined the morphology and distribution of 51 concentric craters. Morphologies of the inner rings vary from donut like, rounded ridges to steep crater rims to flattened mounds. 70% of concentric craters are located near the marginis of maria both on the maria and on the adjacent highlands. They are not found in the central region of maria. Wood (1978) argues that the concentration of concentric craters near mare marginis suggests an association with volcanism and possible association with basin related fractures. However one theory suggests that concentric craters are normal impact craters that developed an inner ring because the impact occurred on a layered surface (usually on thin mare lava), with the

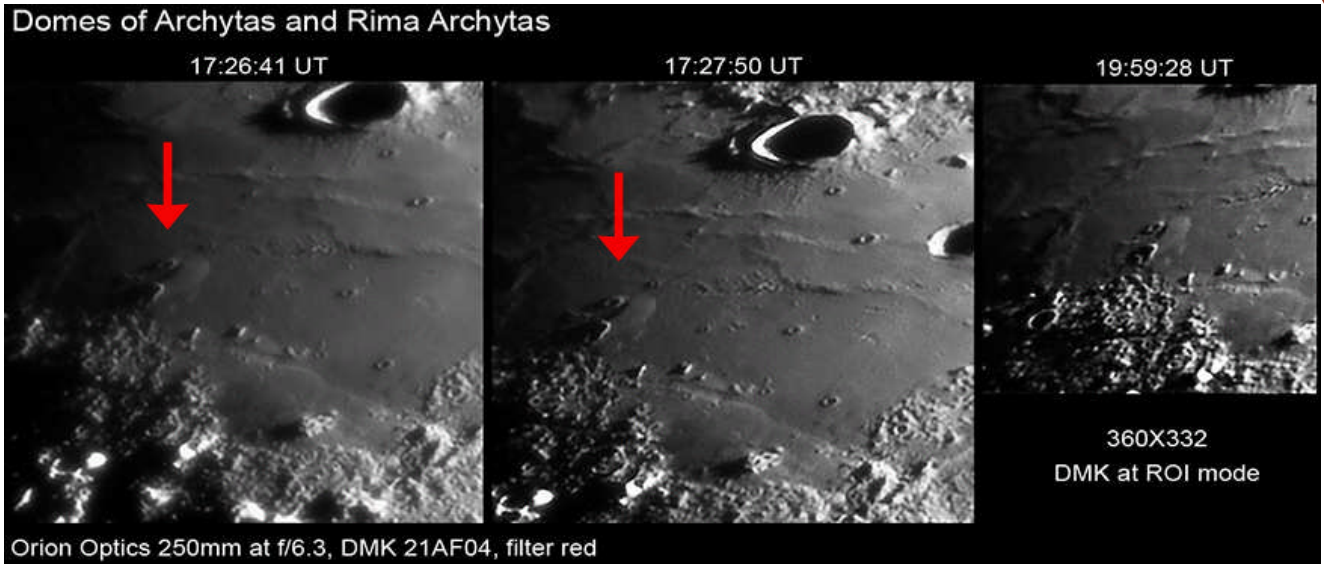
Domes of Archytas and Rima Archytas
17:26:41 UT
17:27:50 UT
19:59:28 UT
360X332
DMK at ROI mode
Orion Optics 250mm at f/6.3, DMK 21AF04, filter red

Fig. 4

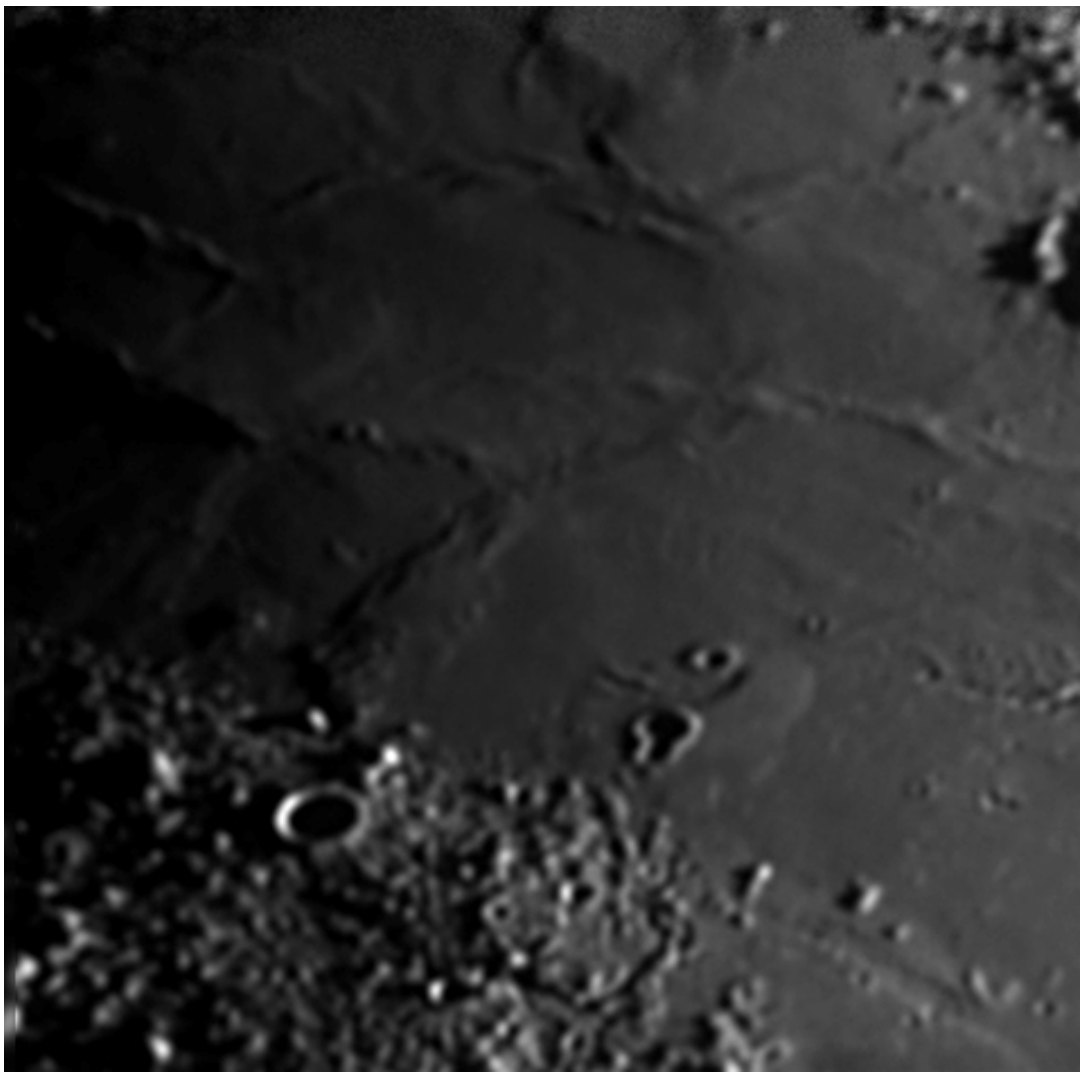

Fig 5

outer rim formed by interaction with the mare and the inner by interaction with the sub-mare layer. A second theory argues that the inner ring forms by some sort of volcanic eruption (Wood, 1978; Wood 2008). The concentric crater Archytas G is situated on raised lava platform (see Fig. 4) with an evident rille-like feature, traversing the surface (cf. description in Section 4.1.1, mapped as an Esc unit in the USGS I-702. It is a cluster or chain of small craters. M'Gonigle and Schleicher (1972) outline evidence of secondary craters and their ejecta excavated by impacts of larger Eratosthenian craters. To the south west another straight rille is situated (see Fig. 9). In the examined region, the ALPO catalogue and the revised list of lunar domes (Kapral and Garfinkle, 2005) report two domes. The first dome described as "double dome" is reported at coordinates of 1.22º E and 55.80º N, with a dimension of 17 km. From our images (see section 4.1) we argue that this dome is a larger shallow structure including the concentric crater Archytas G. Moreover we have identified another dome, of 11 km in diameter, which is not corresponding for dimension (2 km) and position to the previously reported object termed "Plato 4" (Kapral and Garfinkle, 2005).

4.1 Telescopic CCD images, morphometric and spectral properties of the domes near Archytas

A shallow dome has been observed near the crater Archytas, here termed Archytas 1 (AR 1). The dome is located at 0.71º E and 55.71º N. The dome was detected on images (Fig. 4) taken by G. Tarsoudis on March, 14 2008 at 17:26 UT, 17:27 UT and 19: 59 UT using a 250 mm Newtonian telescope and an DMK 21AF04 camera.

The image shown in Fig. 5 displays two domes: the mentioned Archytas 1 and another dome located to the west at 2.71° W and 56.52° N, termed Archytas 2 (AR 2). This image was made by J. Phillips on June 23, 2007 at 01:25 UT (Fig. 5) using a 203 mm TMB apochromatic refractor and an Atik B&W camera.

The images shown in Figs. 6 and 7 were taken by R. Lena in two different sessions carried out on February, 14 2008 at 20:27 UT and April, 13 2008 at 20:55 UT using a 180 mm Maksutov Cassegrain and a Lumenera LU075M.

Figure 7b shows the same image of Fig. 7 but at high focal, made on April, 13 2008 at 21:35 UT.

4.1.1 Dome Archytas 1 (AR 1)

Archytas 1 requires a specific solar altitude to be observed clearly, "disappearing" under higher illumination angles. Interestingly, the concentric crater Archytas G appears to be situated on the summit of the domical structure. The two rilles traversing its surface and the concentric crater are well recognisable in the Clementine image shown in Fig.8. We suggest that this dome includes the concentric crater. Using our available images, the diameter of Archytas 1 amounts to 33 km ± 1 km (cf. Table 1).

The northern part of the dome is traversed by a rille which is composed of multiple craterlets instead of being continuos (see Fig. 8 and Fig . 9 marked with blue arrows). Our interpretation is that the rille is a cluster or chain of secondary craters. Another straight rille (cf. Fig. 8 and the green arrow in Fig. 9) is situated on the southern part of its surface. It ends where the dome reaches the mare surface. Our interpretation is that this straight rille is due to tensional stresses, indicating structural control by subsurface geology. Furthermore, the dark feature detectable near the centre of Archytas 1 just north of the concentric crater is interpreted as a fault extending in north-south direction (cf. Figs. 4-5). Several examples of faults located in the surface of mare-traversing low swells of intrusive nature appear on the Moon. In Fig. 10 we show a fault traversing a low swell to the east of the well-known Valentine Dome (Lena and Wöhler, 2008, Wöhler et al., 2006). This image was taken by J. Phillips on January 14, 2008. Another high-resolution image of the Valentine dome, Apollo 15 Metric Camera image AS15-91-12372, was recently released by the Lunar and Planetary Insitute, Houston (Wood, 2007).

The presence of the fault on the surface of Archytas 1 suggests that its uplift resulted from the rise of magma that did not erupt onto the surface, producing a vertical rupture of the surface. As visible in Figure 8, the relative depth of the concentric crater (Archytas G) appears to be different to that of the small crater to its north, as recognisable from the shadow cast by the rim in this image. Furthermore it has a rim raising above the surrounding mare. However, in the concentric crater the inner ring looks somewhat more degraded than the main rim. This would argue that the inner and outer rims were not formed at the same time.

Fig. 11 displays the colour ratio image from Clementine imagery. The spectral signature of the concentric crater is the same as that of the highland area located to the south. If it is of impact origin, the impact may have excavated highland terrain from below the lava layer of Mare Frigoris. However, an intrusive origin for this large dome (crustal material on top, pressurised magma below, crustal material again under the magma) might also have generated the "layered target" on which the concentric crater then formed by a later impact. Further morphometric data were obtained by a photoclinometric analysis (Horn, 1989; Carlotto, 1996; Wöhler et al., 2006; Lena et al., 2006 and references therein). Using the images shown in Figs. 5 and 7 the dome height amounts to 70 ± 10 m, yielding an average flank slope of 0.25° ± 0.10°. Since we were not able to reconstruct the complete dome surface due to the very bright small fresh impact crater near its summit, we assumed a typical form factor of f = 1/2, which yields an estimated volume of V = 22.4 km³ based on the dome diameter D and height h given in Table 1. The Clementine UVVIS spectral data of the dome Archytas 1 (location marked with a red circle in Fig. 9) reveal a 750 nm reflectance of R_{750} = 0.1485, an extraordinarily low value for the UV/VIS colour ratio of R_{415}/R_{750} = 0.5553, indicating a low TiO_2 content, and a

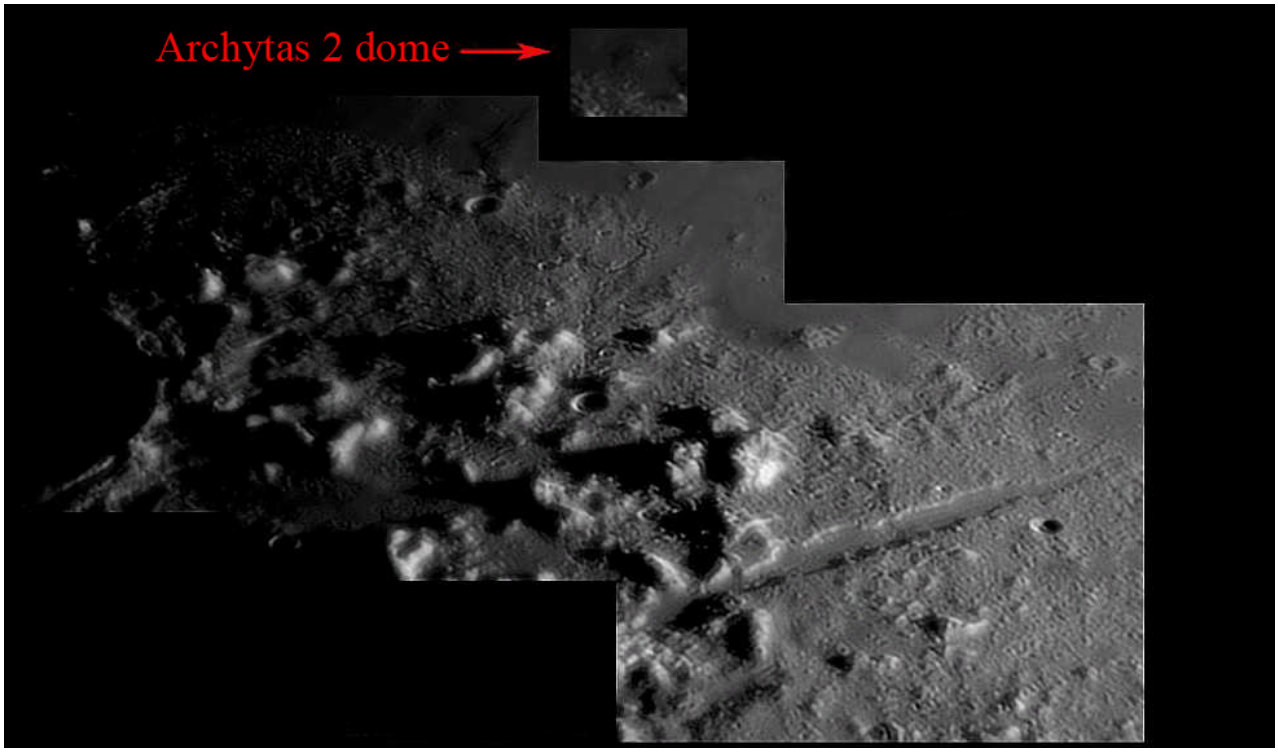

Fig. 6

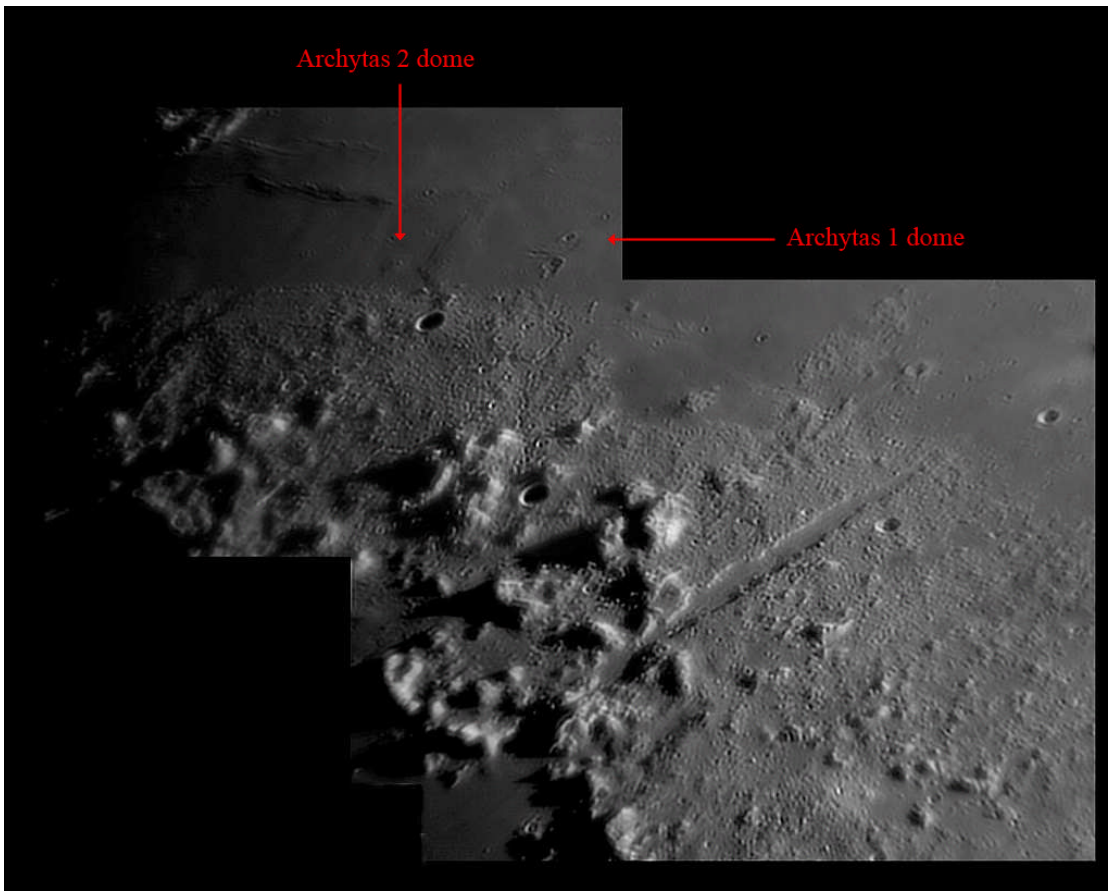

Fig. 7

strong mafic absorption with R_{950}/R_{750} = 1.00159, likely due to the fresh material excavated by the impacts of nearby craters according to multispectral data reported by Whitford-Stark (1990). Clementine UVVIS imagery (Fig. 11) reveals that the surface near the concentric crater, like the nearby highland area to the south, spectrally appear extremely red.According to our preceding studies (Lena and Wöhler, 2008) we interpret this dome to be of intrusive nature due to its large diameter, very low flank slope, and the presence of a straight rille and fault on its surface.

4.1.2 Dome Archytas 2 (AR 2)

Another dome, termed Archytas 2, was detected in the images shown in Figs. 5-7. The different character of this dome is easily recognisable because of the western flank of the dome does show a black shadow. As visible in Figs. 5, 6, 7 and 12 (LO-IV-116-H1) some prominences, presumably non-volcanic hills, are situated on the dome Archytas 2.

Based on the images shown in Figs. 5-7, the height of dome was determined to 265 ± 30 m, resulting in an average slope of 2.7° ± 0.10°. The diameter amounts to 11± 0.4 km. It has been also estimated using the Lunar Orbiter imagery LO-IV-116-H1 (Fig. 12). The scale is 85 m per pixel computed based on crater Plato H of 11 km. We obtained the dimension of 11± 0.08 km for the dome Archytas 2.

The dome volume V was computed by integrating the reconstructed 3D profile over an area corresponding to a circular region of diameter D around the dome summit. A rough quantitative measure for the shape of the dome is given by the form factor $f = V/[\pi h(D/2)^2]$, where we have f = 1/3 for domes of conical shape, f = 1/2 for parabolic shape, f = 1 for cylindrical shape, and intermediate values for hemispherical shape. As much of the dome surface is covered by shadow in our images, the dome volume V was estimated by assuming a form factor of f = 1/2, which yields an edifice volume of 12.6 km^3. Using the shadow length method, a dome height of 260 ± 30 m was obtained from Fig. 6.

The Clementine UVVIS spectral data of the dome AR 2 reveal a 750 nm reflectance of R_{750} = 0.14234, an extraordinarily low value for the UV/VIS colour ratio of R_{415}/R_{750} = 0.5394, indicating a low TiO_2 content and a strong mafic absorption with R_{950}/R_{750} = 1.0140, likely due to the fresh material excavated by the impacts of nearby craters (see location marked with a red circle in Fig. 9)

For its morphometric properties, e.g height and slope, we interpret this dome of effusive origin. Wöhler et al. (2006) introduce an extension of the definitions of classes 1-3 of the scheme by Head and Gifford (1980). They base the distinction between these shield-like volcanoes on their associated spectral and morphometric quantities. Four classes termed A, B, C, and E describing monogenetic mare domes are established essentially according to the diameter, flank slope, volume of the dome edifice and the TiO_2 content of its soil. Lena (2007) formulates this scheme

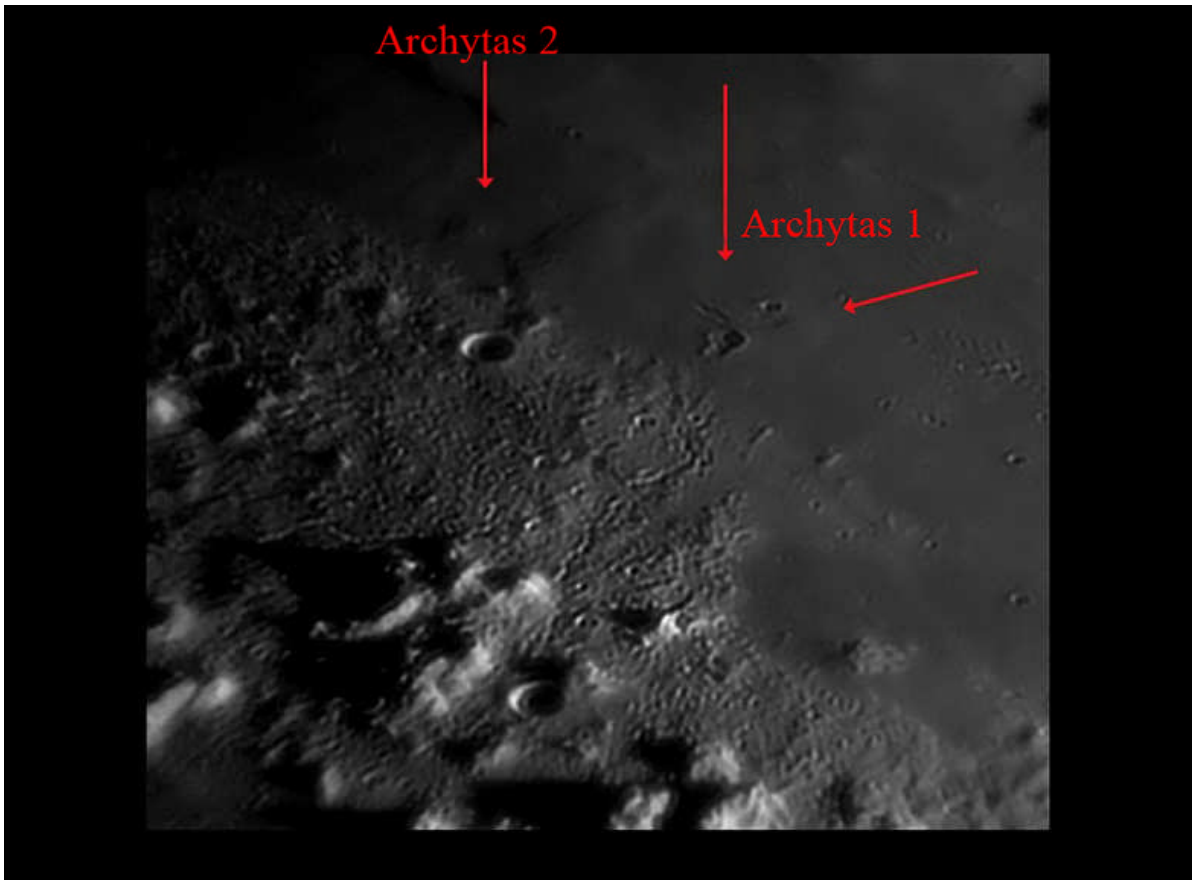

Fig. 7b

as a flow chart, additionally taking into account the rheologic properties of the dome-forming lava (cf. also Wilson and Head, 2003).

The model by Wilson and Head (2003) estimates the yield strength τ, i. e. the pressure or stress that must be exceeded for the lava to flow, the plastic viscosity η, yielding a measure for the fluidity of the erupted lava, the effusion rate E, i. e. the lava volume erupted per second, and the duration T = V/E of the effusion process.

The computed values for τ, η, E and T obtained are valid for domes that formed from a single flow unit (monogenetic volcanoes).

The rheologic model by Wilson and Head (2003) yields for the dome Archytas 2 an effusion rate of 119 m^3/s. It was formed from lava of viscosity of 4.4 x 10^6 Pa s, over a period of time of 3.4 years (Table 2).

5. Results and discussion

We have examined two lunar domes in Mare Frigoris and another dome in Mare Imbrium, near crater C. Herschel in terms of their spectral and morphometric properties and the eruption conditions encountered during their formation.

5.1 Effusive dome Archytas 2 (AR 2). Eruption conditions and mode of emplacement

Based on the spectral and morphometric data obtained in this study, the comparably steep dome Archytas 2 belongs to class B1 in the scheme introduced by Wöhler et al. (2006) and later refined by Lena (2007). It consists of lavas of intermediate to high viscosity and low TiO2 content, erupting at intermediate effusion rates. If the effusion process continues over a long period of time, steep flank slope and high edifice volume may occur as in the case of Archytas 2 (class B1), while short durations of the effusion process result in lower edifices of lower volume, as it is the case for the domes belonging to class B2 (Wöhler et al, 2006; Wöhler et al, 2007; Lena et al, 2007; Lena et al, 2008).

Wöhler et al. (2007) establish three rheologic groups of effusive lunar mare domes.

The first group, R1, is characterised by lava viscosities of 10^4-10^6 Pa s, magma rise speeds of 10^{-5} – 10^{-3} m s^{-1}, dike widths around 10-30 m, and dike lengths between about 30 and 200 km. Rheologic group R2 is characterised by low lava viscosities between 10^2 and 10^4 Pa s, fast magma ascent (U > 10^{-3} m s^{-1}), narrow (W = 1-4 m) and short (L = 7-20 km) feeder dikes.

The third group, R3, is made up of domes which formed from highly viscous lavas of 10^6- 10^8 Pa s, ascending at very low speeds of 10^{-6} – 10^{-5} m s^{-1} through broad dikes of several tens to 200 m width and 100- 200 km length. The dome Archytas 2 is a typical representative of rheologic group R3.

It is characterised by lava viscosity of about 10^6 Pa s, with computed magma rise speed of 4.4 x 10^{-6} m s^{-1}, dike width

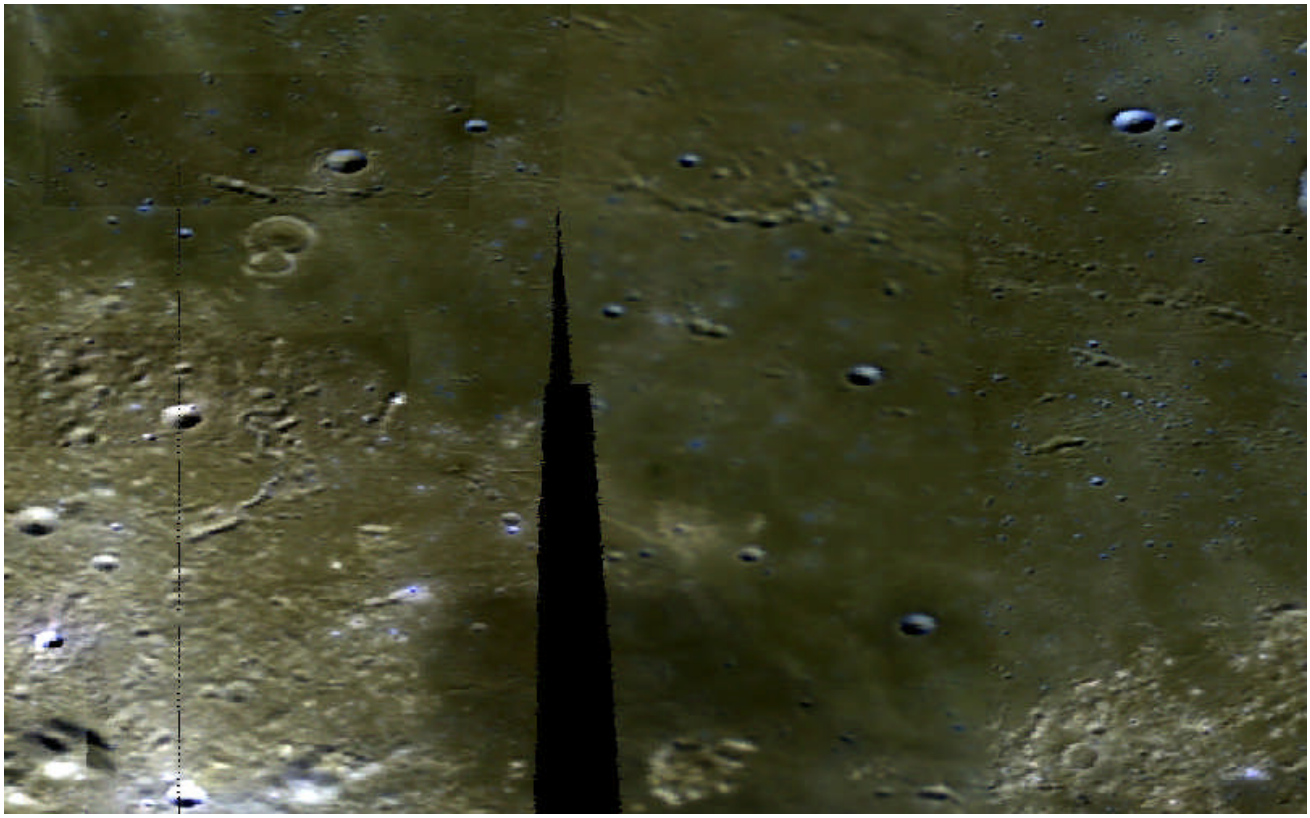

Fig. 8

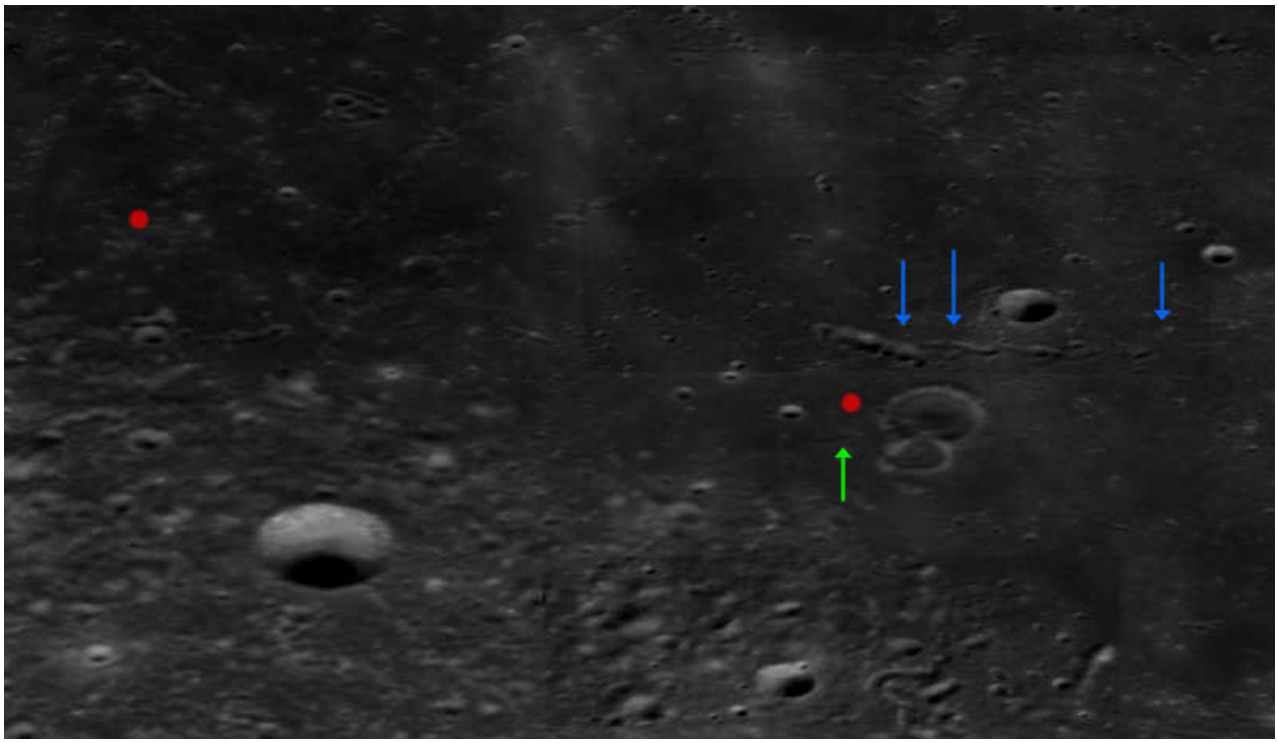

Fig. 9

of 114 m and dike length of 178 km.

Archytas 2 has small positive reliefs on the surface, well visible in the Lunar Orbiter image in Fig. 12. They likely represent pre-existing small peaks surrounded by the dome. A lunar mare dome that comes close to Archytas 2 is the steep dome Condorcet 4 in Mare Undarum (Lena et al, 2008). Condorcet 4 has positive reliefs on the surface. Its effusion rate amounts to 102 m^3 s^{-1}, similar to the value of 119 m^3 s^{-1} determined for Archytas 2. The estimated duration of the effusion time is of 3.4 and 4.2 years for Archytas 2 and Condorcet 4, respectively. We found that the feeder dike of Condorcet 4 has length of 178 km (170 km for Archytas 2), indicating an origin of the dome-forming magma well below the lunar crust (cf. Lena et al, 2008). The width of the dike estimated for Archytas 2 of 114 m is also comparable with the dike wide of 84 m inferred for Condorcet 4.

The viscosity of the lava that formed Archytas 2 of 4.4 x 10^6 Pa s is also comparable to the values derived for other representative domes of rheologic group R3, e. g. Herodotus ω, but about a factor of three lower than the viscosities inferred for Hortensius 5 and 6 and Doppelmayer 1 belonging to the same class B1 (Lena et al, 2008). We suggest that these differences were probably caused by a somewhat higher eruption temperature occurring for the dome Archytas 2 and thus a lower crystallinity of the lava.

5.2 Intrusive domes Archytas 1 (Ar1) and dome C. Herschel 1 (CH 1) of unknown origin

In this study we have examined two further lunar domes, displaying different morphometric properties. Archytas 1 is interpreted to be an intrusive structure due to the presence of a short straight rille and a fault traversing the surface, suggesting that its uplift resulted from the rise of magma that did not erupt onto the surface, producing a vertical rupture of the surface. A rille is also detectable on the surface of the low dome C. Herschel 1.

Archytas 1 is a large and voluminous structure, compared to other lunar domes of intrusive origin (cf. Lena and Wöhler, 2008). Table 3 reports the flank slope, diameter, height, and edifice volume of Archytas 1 along with data of the dome Palmieri 1 (Lena et al., 2008) and further intrusive domes described in our preceding studies.

Lena et al. (2008) establish three classes of intrusive mare domes. The first group, In 1, is characterised by domes with large diameters, high edifices volumes, and straight rilles or faults traversing their surface. The domes Archytas 1, as Gambart 1 (Ga1), the Valentine dome (V1), and M13 belong to this group. We suggest that during the formation of the large intrusive domes of class In1 fracturing and faulting of the crust occurred, weakening the strength of the crust and thus facilitating the uplift of large volumes of crustal material visible as a large intrusive dome. Some domes of this group (Ga 1, V1 and M13) have pre-existing small peaks. The presence of the fault on the summit of Archytas 1 suggests that the uplift resulting from the rise of magma produced a vertical rupture of the

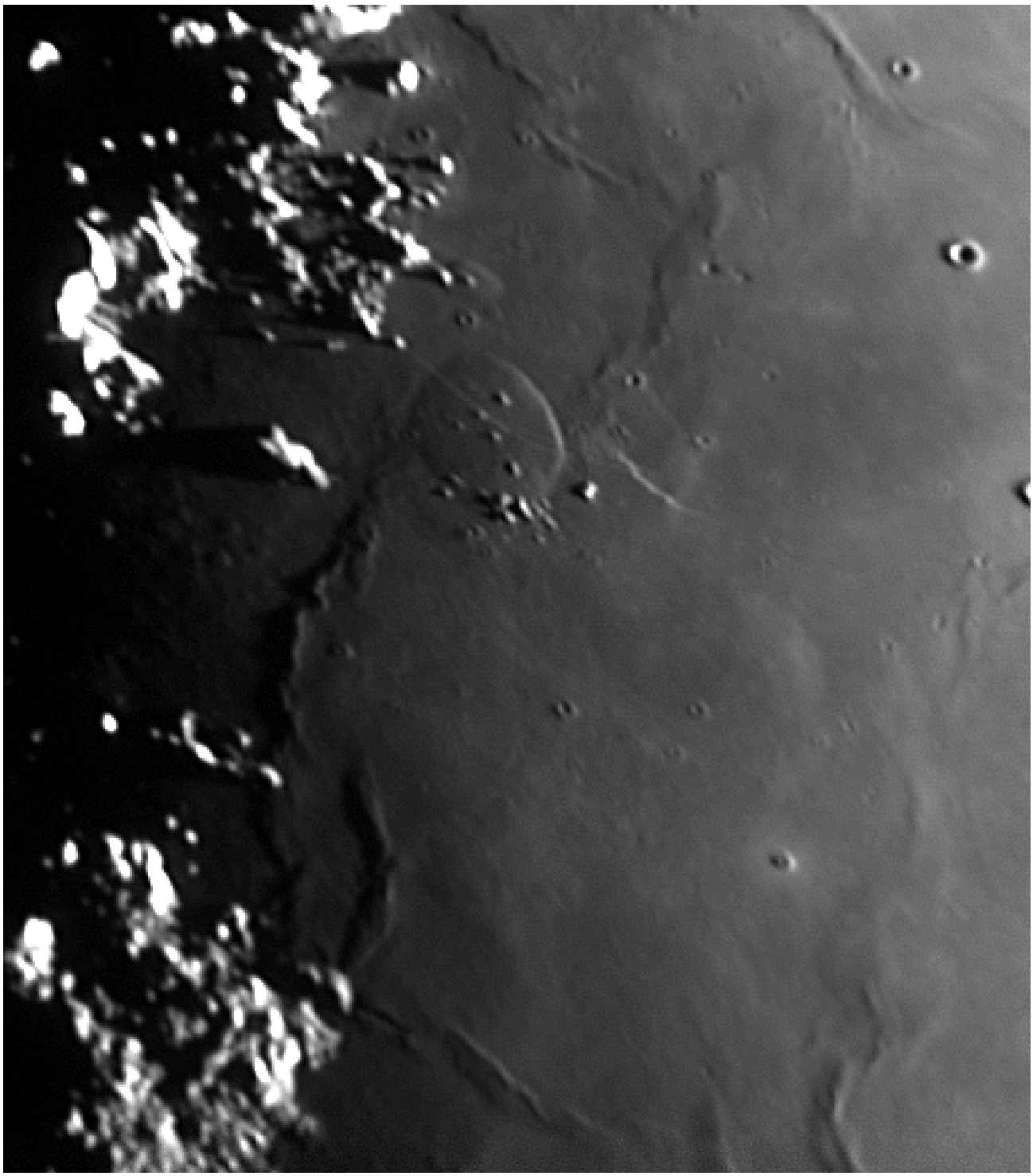

Fig. 10

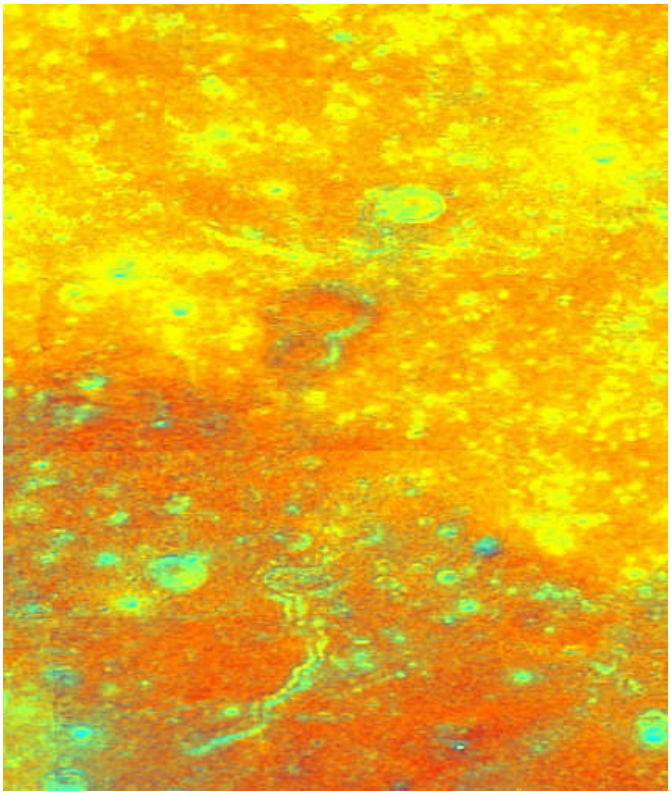

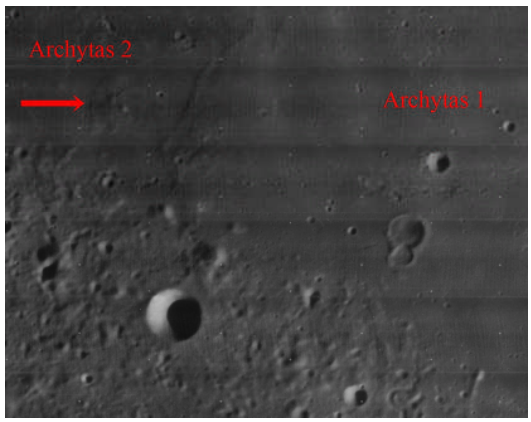

Fig. 12

Fig. 11

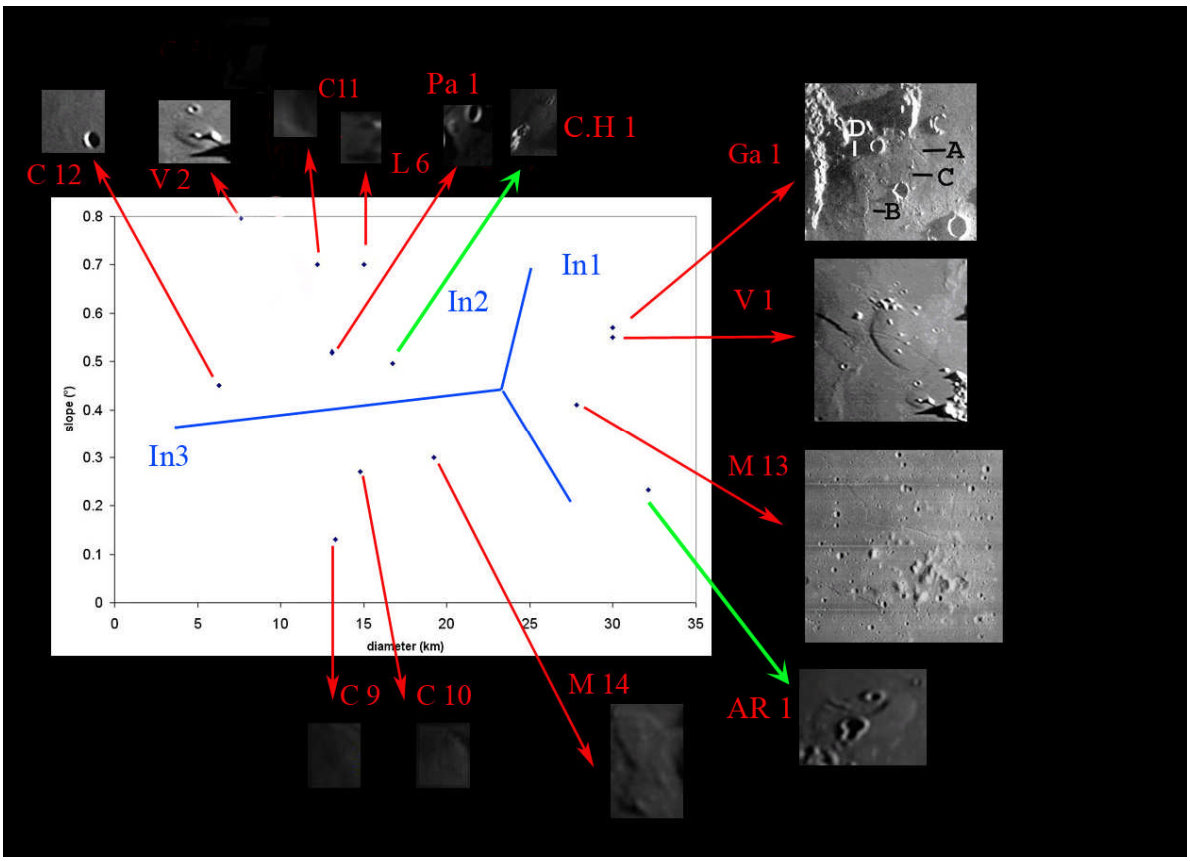

Fig. 13

Table 1: properties of the three domes examined in this study.

dome	Long [°]	Lat [°]	Heigth [m]	Slope [°]	D [km]	V [km^3]	Remarks (Class)
C. Herschel 1 (CH 1)	-32.57°	34.76°	64	0.44	16.8	7.1	undefined
Archytas 1 (AR 1)	0.71°	55.71°	70	0.25	33.0	22.4	Intrusive
Archytas 2 (AR 2)	-2.71°	56.52°	265	2.70	11.0	12.6	Effusive

Table 2: rheologic properties of Archytas 2 and further domes of Class B1 from our preceding studies (*).

dome	Long [°]	Lat [°]	η [Pa s]	E [m^3 sec^{-1}]	T [years]	U [m sec^{-1}]	W [m]	L [km]
Archytas 2 (AR 2)	-32.57°	34.76°	4.4 x 10^6	119	3.4	4.4 x 10^{-6}	114	170
Condorcet 4 (Co4)	70.93°	6.67°	5.2 x 10^6	102	4.8	6.8 x 10^{-6}	84	178
Doppelma-yer 1 (Do1)	-41.92°	-30.08	1.4 x 10^7	121	8.9	5.7 x 10^{-6}	127	167

(*) The height and slope for Condorcet 4 is of 270 m and 2.80°. The height and slope for Doppelmayer 1 is 410 m and 2.8°.

Table 3. Morphometric properties of some intrusive domes

Dome	Long.	Lat.	slope [°]	D [km]	h [m]	V [km^3]	Class
AR 1	0.71°	55.71°	0.25	33	70	22.4	In 1
Pa1	-47.88°	-26.63°	0.50	13.5	60	4.3	In 2
Ga1	-14.84°	-0.75°	0.57	30	140	50	In 1
L6	-29.16°	47.08°	0.70	10	95	1.5	In 2
V1	10.20°	30.70°	0.55	30	130	42	In 1
V2	10.26°	31.89°	0.82	11	80	1.9	In 2
C9	34.66°	7.06°	0.13	13.3	15	0.5	In 3
C10	35.19°	10.00°	0.30	19.2	50	10	In 3
C11	36.75°	11.06°	0.70	12.2	75	6.4	In 2
C12	37.20°	12.37°	0.45	6.3	25	0.5	In 2
M13	-31.53°	11.68°	0.41	27.8	100	15	In 1
M14	-32.13°	12.76°	0.27	14.8	35	1.7	In 3
CH 1	-32.57°	34.76°	0.44	16.8	64	7.1	C1 (or In2)

surface. As a note of interest, Archytas 1 represents the first lunar dome known to date with a concentric crater in its surface.

The second class, In2, is characterised by domes with moderate diameters (range of 10 to 20 km) and low or moderate edifice volumes (0.5-7 km^3). Only the dome C12 shows a smaller diameter of 6.3 km. Class In2 is also characterised of domes with slope in the range of 0.41° to 0.82° and height in the range of 25-80 m. Some domes of class In2 have small hills on their surface. If it was assumed to be of intrusive origin, the dome C. Herschel 1 could be assigned to class In2. Regarding it as an effusive dome would imply to assign it to the effusive class C1. In this scenario the circularity of the dome of 0.97 should be attributed to an effusive construct.

The third class of intrusive domes, In3, is made up of structures with lower flank slopes than those comprised by class In2. From our available data we have produced the diagram shown in Fig. 13, displaying the slope versus diameter of the intrusive domes reported in Table 3, including as preliminary data also CH1 if it is of intrusive nature, also if its circularity is evident as for effusive mare domes.

Future work will include an extension of our analysis to further intrusive domes, and to infer, with more analysis, "morphometric borders" between the object classes of intrusive and effusive domes. Such studies will help to gain more detailed insight into the global and regional internal geologic processes responsible for the formation of the observed various types of lunar mare domes and intrusive domes on the moon.

Acknowledgements: We wish to thank C. Wöhler for his comments and suggestions to this paper.

References

[1] Charette, M. P., McCord, T. B., Pieters, C. M., Adams, J. B., 1974. Application of remote spectral reflectance measurements to lunar geology classification and determination of titanium content of lunar soils. J. Geophys. Res. 79, 1605-1613.

[2] Carlotto, M.J. 1996. Shape From Shading.

http://www.newfrontiersinscience.com/

martianenigmas/Articles/SFS/sfs.html
(last date accessed: 19 Feb. 2007)

[3] Eliason, E., Isbell, C., Lee, E., Becker, T., Gaddis, L., McEwen, A., Robinson, M., 1999. Mission to the Moon: the Clementine UVVIS global mosaic. PDS Volumes USA NASA PDS CL 4001 4078. http://pdsmaps.wr.usgs.gov

[4] Gillis, J. J., Lucey, P. G., 2005. Evidence that UVVIS ratio is not a simple linear function of TiO_2 content for lunar mare basalts. Lunar Planet. Sci. XXXVI, abstract #2252.

[5] Head, J. W., Gifford, A., Lunar Domes: Classification and Modes of Origin, Moon and Planets, vol. 22, pp. 235-258, 1980.

[6] Horn, B. K. P., 1989. Height and Gradient from Shading. MIT technical report 1105A. http://people.csail.mit.edu/people/bkph/AIM/AIM-1105A-TEX.pdf

[7] Kapral, C., Garfinkle, R., 2005. GLR Lunar Dome Catalog. http://www.glrgroup.org/domes/kapralcatalog.htm

[8] Lena, R., Wöhler, C., Bregante, M.T, Fattinnanzi, C. 2006. A combined morphometric and spectrophotometric study of the complex lunar volcanic region in the south of Petavius. Journal of the Royal Astronomical Society of Canada, vol. 100, no. 1, 14-25.

[9] Lena, R., Wöhler, C., Phillips, J., Wirths, M., Bregante, M.T. 2007. Lunar domes in the Doppelmayer region: Spectrophotometry, morphometry, rheology, and eruption conditions. Planetary and Space Science, vol. 55, 1201-1217.

[10] Lena, R., 2007. Lunar Domes Classification and Physical Properties. Selenology Today, 5, pp. 62-78.

[11] Lena, R., Wöhler, C., Bregante, M.T, Lazzarotti, P., Lammel, S., Lunar domes in Mare Undarum: Spectral and morphometric properties, eruption conditions, and mode of emplacement. Planetary and Space Science, vol. 56, 3-4, pp. 553-569.

[12] Lena, R., Wöhler, C. Intrusive Lunar Domes: Morphometry and Mode of Emplacement. Lunar and Planetary Science Conference XXXIX, abstract #1122, League City, Texas, 2008.

[13] Lena, R., Wöhler, C., Phillips, J., Bregante, M. T., Benavides, R., 2008. A lunar dome near Palmieri crater and the properties of intrusive lunar domes. Selenology Today 10, pp. 4-14.

[14] Lucchitta, B. K., 1972. Geologic Map of the Aristoteles Quadrangle of the Moon. US. Geol. Sur. Misc. Invest. Ser. Map 1-725.

[15] Lucchitta, B. K., 1978. Geologic Map of the North Side of the Moon. U.S. Geol. Sum. Misc. Invest. Set. Map 71062.

[16] Lucchitta, B. K. and Watkins, J. A.,1978. Age of graben systems on the Moon. Proc. Lunar Planet. Sci. Conf. 9th, pp. 3459-3472.

[17] Lucey, P. G., Blewett, D. T., Hawke, B. R. 1998. Mapping the FeO and TiO_2 content of the lunar surface with multispectral imagery. J. Geophys. Res. 103(E2), 3679-3699.

[18] M'Gonigle, J. W. and Schleicher, D. 1972. Geologic Map of the PlatoQuadrangle of the Moon. US. Geol. Sure. Misc. Invest. Ser Map I-701.

[19] Mosher, J., Bondo, H., 2006. Lunar Terminator Visualization Tool (LTVT).

http://inet.uni2.dk/ d120588/henrik/jimltvt.html

[20] Schaber, G. G., Geologic Map of the Sinus Iridum Quadrangle of the Moon, USGS, Lunar geologic map I-602, 1969.

[21] Spudis, P. D., Hawke, B.R, and Lucey, P. G., 1988. Materials and formation of the Imbrium basin. Proc. Lunar Planet. Sci. Conf. 18th, pp. 155-168.

[22] Spudis ,P.D., 1993. Geology of Multi-ring Basins, Cambridge Univ. Press.

[23] Spudis, P. D., Bussey, D.B.J., Hawke, B.R, 1999. Deposits of the Imbrium Basin: Montes Alpes and Caucasus. Lunar and Planetary Science XXX, 1999, 1348.pdf

[24] Ulrich, G. E., 1969. Geologic map of the J. Herschel Quadrangle of the Moon. U.S. Geol. Sure. Misc. Invest. Ser Map 1604.

[25] Wilhelms, D., 1987. The geologic history of the Moon. USGS Prof. Paper 1348.

[26] Whitford-Stark J. L and Head J. W. (1980) Stratigraphy of Oceans Procellarum basalts: Sources and styles of emplacement. J Geophys. Res, 85, 6579-6609.

[27] Whitford-Stark, J.L., 1993. Frigoris Revisited. Lunar and Planetary Science XIV, pp. 843-844.

[28] Whitford-Stark, J.L., 1990. The Volcanotectonic Evolution of Mare Frigoris. Proc. Lunar Planet. Sci. Conf. 20th, pp. 175-185.

[29] Wilson, L., Head, J. W., 2003. Lunar Gruithuisen and Mairan domes: Rheology and mode of emplacement, J. Geophys. Res. 108(E2), pp. 5012-5018.

[30] Wöhler, C., Lena, R., Lazzarotti, P., Phillips, J., Wirths, M., Pujic, Z. 2006. A combined spectrophotometric and morphometric study of the lunar mare dome fields near Cauchy, Arago, Hortensius, and Milichius. Icarus, vol. 183, 2, 237-264.

[31] Wöhler, C., Lena, R., Phillips, J. Formation of lunar mare domes along crustal fractures: Rheologic conditions, dimensions of feeder dikes, and the role of magma evolution. Icarus, vol. 189, no. 2, pp. 279-307, 2007.

[32] Wood, C. A., Lunar Concentric Craters. 1978. Lunar and Planetary Science IX, pp. 1264-1266.

[33] Wood, C.A, LPOD, 2007 http://lpod.org/coppermine/displayimage.php?pos=-1675

[34] Wood, C.A, LPOD, 2008. Two New/Old Concentric Craters http://the-moon.wikispaces.com/LPOD+Mar+30%2C+2008

Spectral Study of Banded Craters Using Clementine 5 Band UVVIS Data

by Richard Evans

Geologic Lunar Research (GLR) Group

Abstract

This study analyzes an eleven crater subset of the 188 banded craters cataloged by Albineri and Lenham in 1955 for mineral composition of crater walls and for central peaks when they were present. Composition was determined by use of absolute reflectance and normalized reflectance plots generated from Clementine 5 band UVVIS data according to the method described by Tompkins (1998). The goal of the analysis was to determine whether or not significant compositional differences might be associated with the radial crater banding observed either visually or photographically.

Introduction

In an article written in the Journal of the British Astronomical Association in 1955, Albineri and Lenham cataloged 188 banded craters on the near side of the moon. This list is still used by amateur astronomers today and currently serves as the most definitive list of banded craters available. Banded craters are craters having radial bands of alternate light and dark albedo in their walls that can be observed either visually or photographically. Albineri and Lenham grouped craters into one of five groups based on their general characteristics and the appearance of their bands. The crater prototypes of Groups 1 through 5, respectively are: Aristarchus, Conon, Messier, Birt, and Agatharchides A. Groups assigned to the banded crater catalog can be found in Appendix 1.

For the most part, these bands are currently felt to be due to landslides which expose fresh material unaffected by the darkening effects of longer term weathering on lunar soil. The present study undertook an analysis of the 5 band Clementine UVVIS spectra of various regions of the walls of cataloged banded craters to determine whether any significant compositional differences could be detected.

Method

A subset of eleven craters in the Albineri and Lenham article was located in the Clementine UVVIS data set available on the USGS Map-a-Planet website at

http://pdsmaps.wr.usgs.gov/PDS/public/explorer/html/moonpick.htm.

The 5 band Clementine UVVIS 16 bit TIFF images at 415 nm, 750 nm, 900 nm, 950 nm, and 1000 nm were downloaded and brought into the program ImageJ as an image sequence. Multiple different areas within the wall of each crater (and central peak areas as well when present) were selected using a user defined pixel box. The greyscale value of the pixel average within the pixel box and the standard deviation was determined using the histogram function in ImageJ. To achieve absolute reflectance, the resulting value was multiplied by 0.000135. Using Excel, plots were made of absolute and normalized reflectance vs wavelength for the 5 band UVVIS data and referenced to the specific region of the crater that was sampled. Based on the shape of the resulting curves, a compositional assessment was made using the method described by Tompkins (1997 & 1998). Absolute reflectance was useful in determining albedo differences between light and dark bands in the crater walls. Normalized reflectance was useful in assessing mafic band depths and could be directly compared to reference spectra for different lunar mineral compositions (Tompkins 1997 and 1998).

Banded Crater Data

1. Schomberger A (Visual Banded Crater)

Clementine Images with Wall Areas Sampled for Spectra

Figures 1a, 1b, 1c and 1d

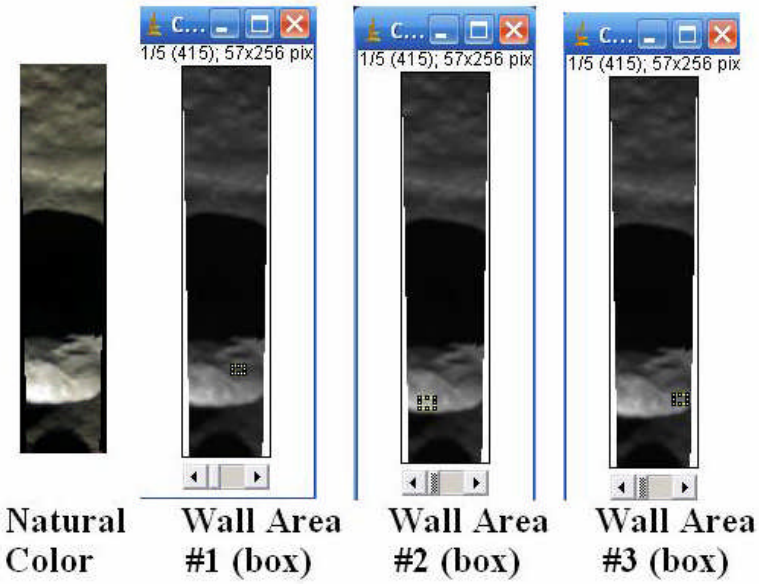

Clementine 5 Band UVVIS Spectra:

Figures 1e and 1f

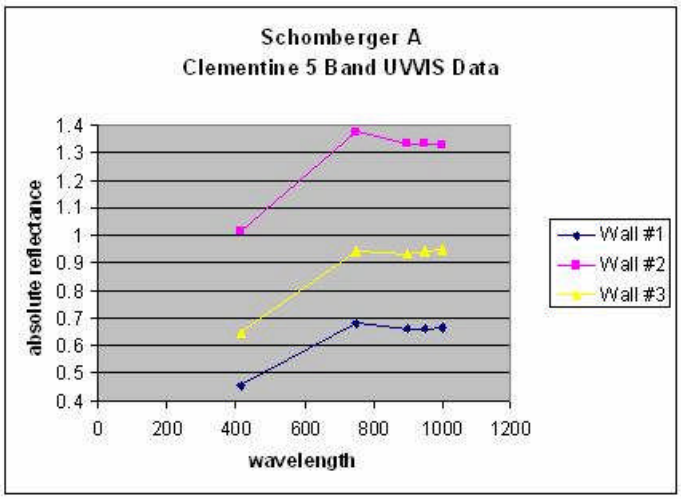

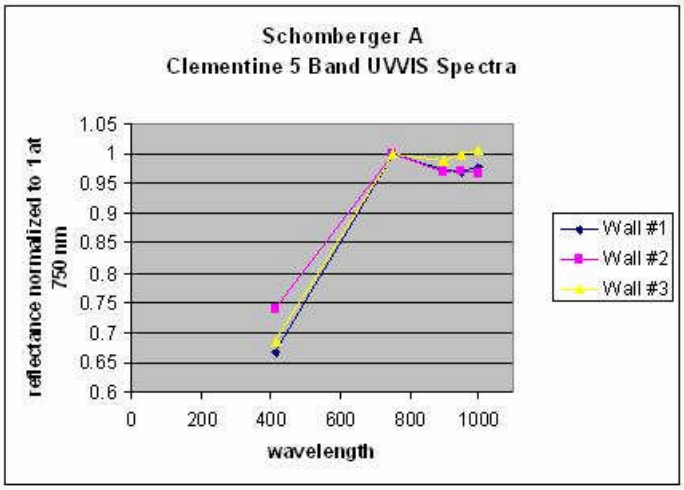

Comparison of Natural Color and Maturation Ratio Images:

Figures 1g & 1h

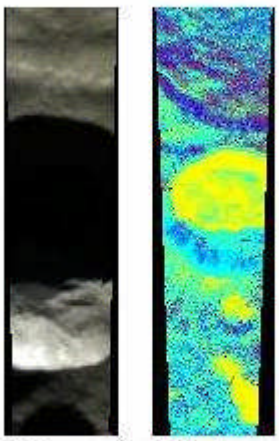

Natural Color | Maturation Ratio

Interpretation of Wall Composition based on Tompkins (1998)

All wall areas sampled have spectra classified as anorthositic, type 2 (An2) based on the shape of the 5 band UVVIS spectral curves shown above. Type 1 anorthosites (An1) are more nearly pure plagioclase feldspars, while the type 2 anorthosites (An2) have a small amount of orthopyroxene (low calcium pyroxene), usually noritic in nature. The darkest band had an albedo that was 50% less than the lightest band at 750 nm.

2. Cichus C (Photographic banded crater)

Clementine Images with Wall Areas Sampled for Spectra

Figures 2a, 2b, 2c and 2d

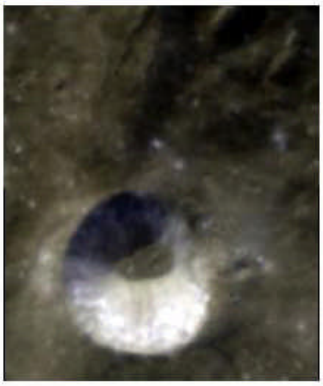

Natural Color

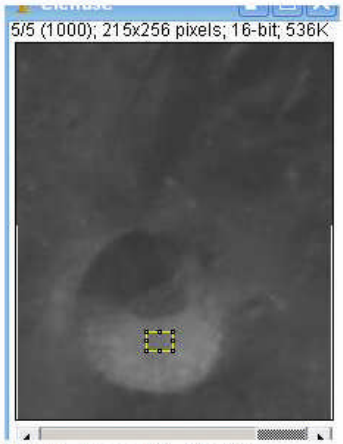

Wall Area #1 (box)

Wall Area #2 (box)

Wall Area #3 (box)

Clementine 5 band UVVIS Spectra

Figures 2e & 2f

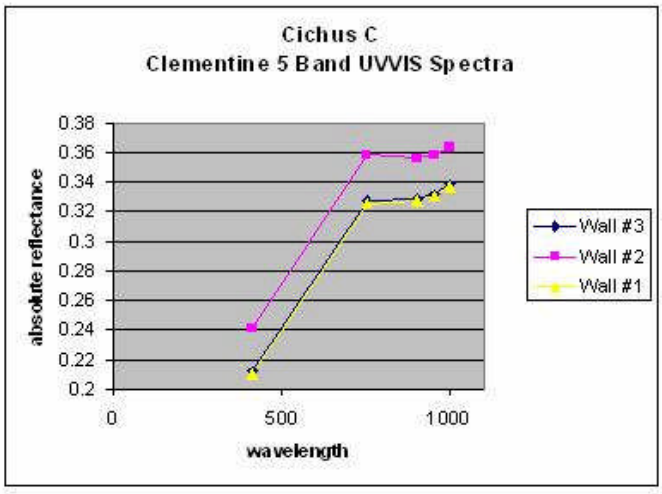

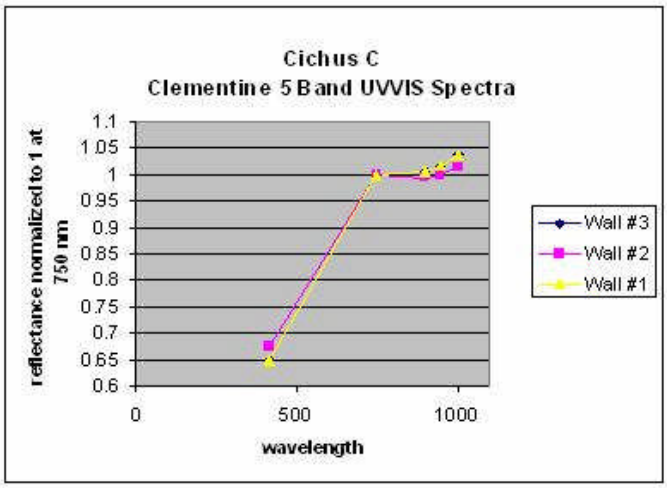

Comparison of Natural Color and Maturation Ratio Images

Figures 2g & 2h

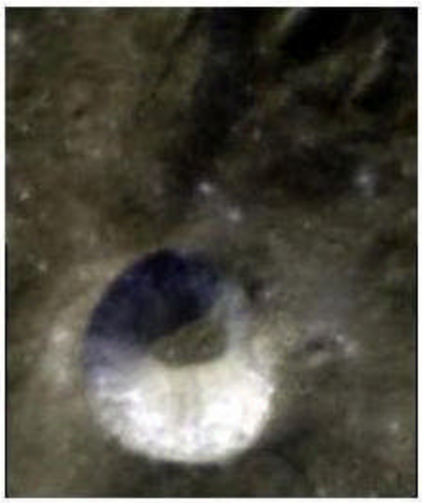

Natural Color

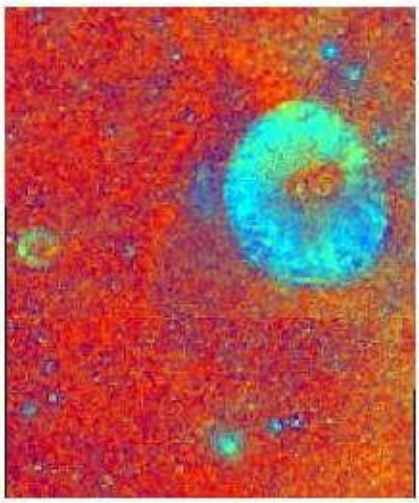

Maturation Ratio

Interpretation of Wall Composition Based on Tompkins (1998)

All wall areas sampled have spectra classified as anorthositic, type An2 based on the shape of the 5 band UVVIS spectral curves shown above. The darkest band had an albedo that was 9.2 percent less than the lightest band at 750 nm. There is a suggestion that darker albedo features in the crater wall on the natural color image might correspond to areas of yellow to yellowish green color (possibly indicating a slightly higher iron content or weathering effects) on the maturation image although it is not definitive.

3. Adams B (Photographic Banded Crater)

Clementine Images with Wall Areas Sampled for Spectra

Figures 3a, 3b & 3c

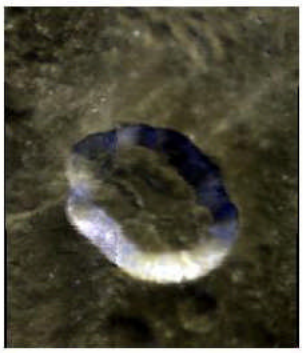

Natural Color

Wall Area #1 (box)

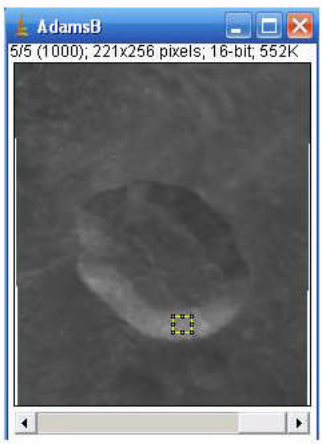

Wall Area #2 (box)

Clementine 5 Band UVVIS Spectra:

Figures 3e & 3f

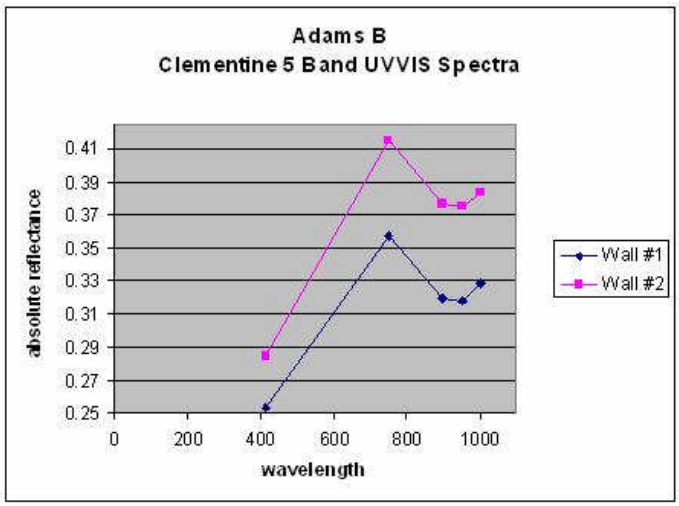

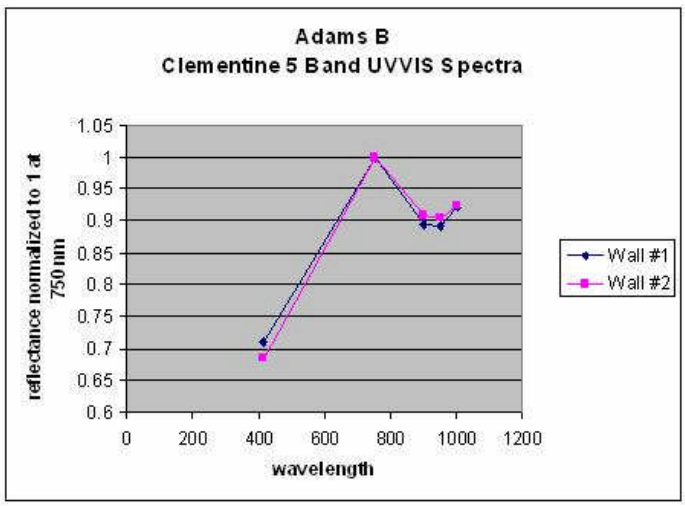

Comparison of Natural Color and Maturation Ratio Images

Figures 3f & 3g

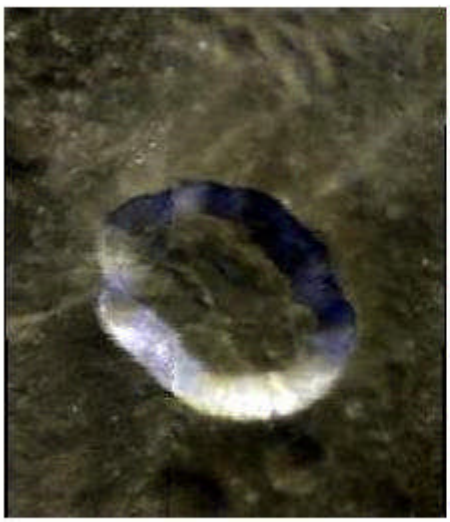

Natural Color

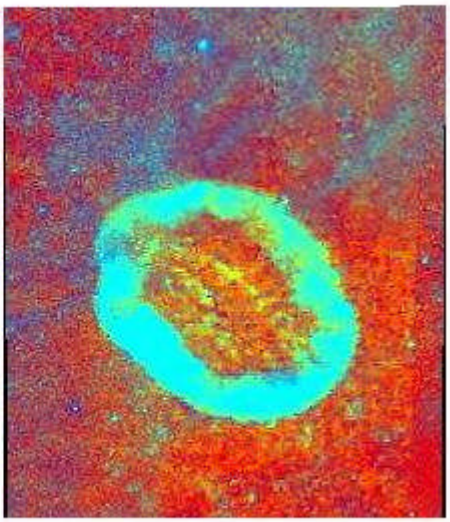

Maturation Ratio

Interpretation

Both wall areas sampled have spectra classified as anorthositic norite (AN) based on the shape and band depth of the 5 band UVVIS spectral curves shown above. The darkest band had an albedo that was 14 percent less than the lightest band at 750 nm. Darker albedo areas have a slightly more yellowish appearance on the maturation image which may indicate a slightly higher iron content or the effects of weathering.

4. Davy A (Photographic Banded Crater)

Clementine Images with Wall Areas Sampled for Spectra

Figures 4a, 4b & 4c

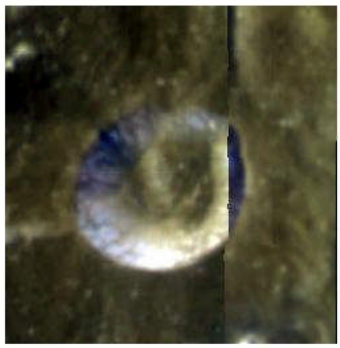

Natural Color

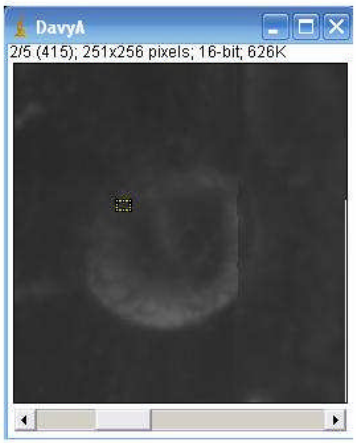

Wall Area #1 (box)

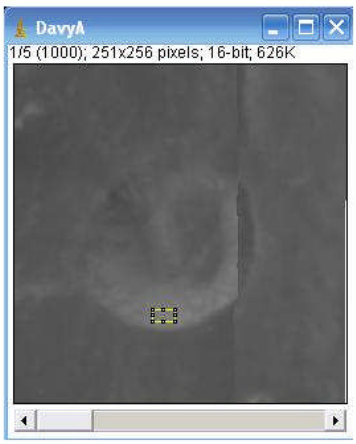

Wall Area #2 (box)

Clementine 5 Band UVVIS Spectra

Figure 4d & 4e

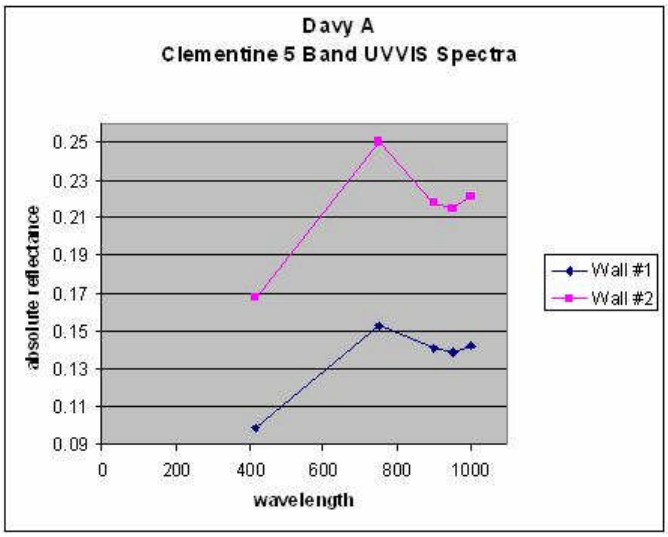

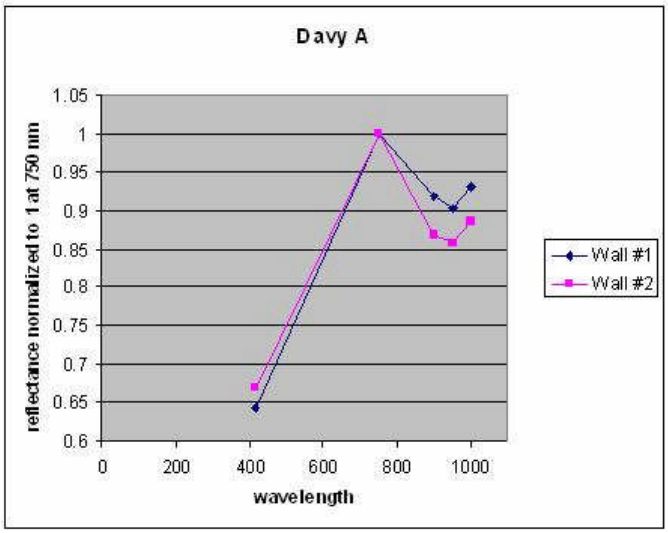

Comparison of Natural Color and Maturation Ratio Images

Figures 4f & 4g

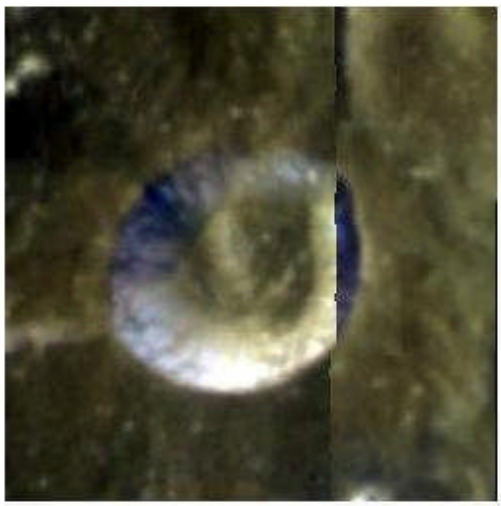

Natural Color

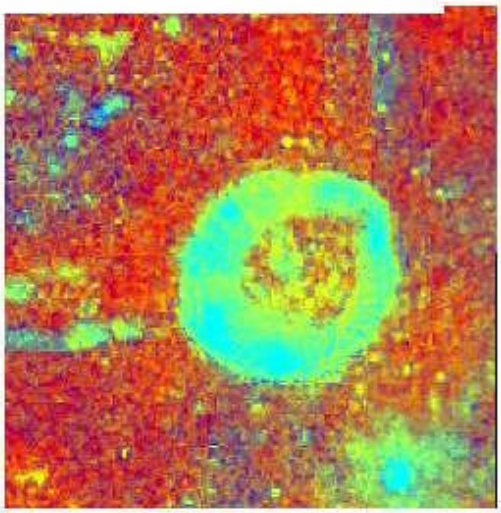

Maturation Ratio

Interpretation based on Tompkins (1998)

Both wall areas sampled have spectra classified as anorthositic norite (AN) based on the shape and band depth of the 5 band UVVIS spectral curves shown above. The darkest band had an albedo that was 39% less than the lightest band at 750 nm. Darker albedo areas appear to have a yellow to yellowish green appearance on the maturation image which may indicate a slightly higher iron content or the effects of weathering.

5. Bohnenberger G (Photographic Banded Crater)

Clementine Images with Wall Areas Sampled for Spectra

Figures 5a, 5b, 5c & 5d

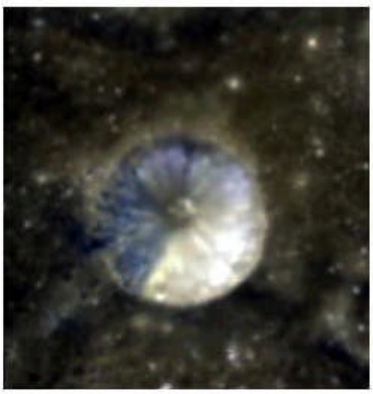

Natural Color

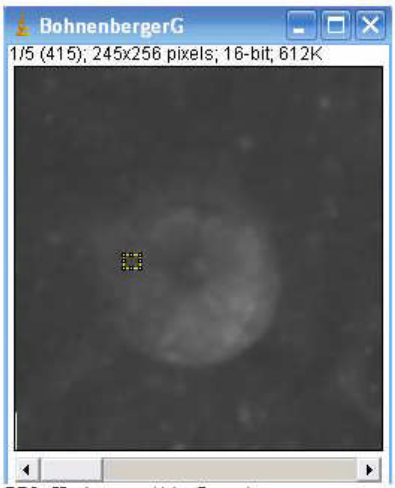

Wall Area #1 (box)

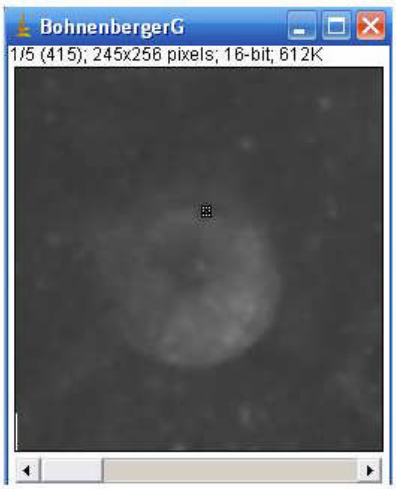

Wall Area #2 (box)

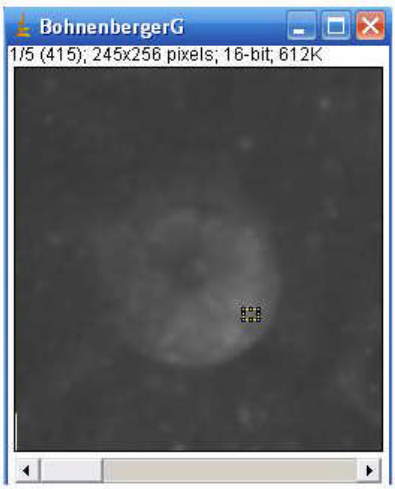

Wall Area #3 (box)

Clementine 5 Band UVVIS Spectra

Figures 5e & 5f

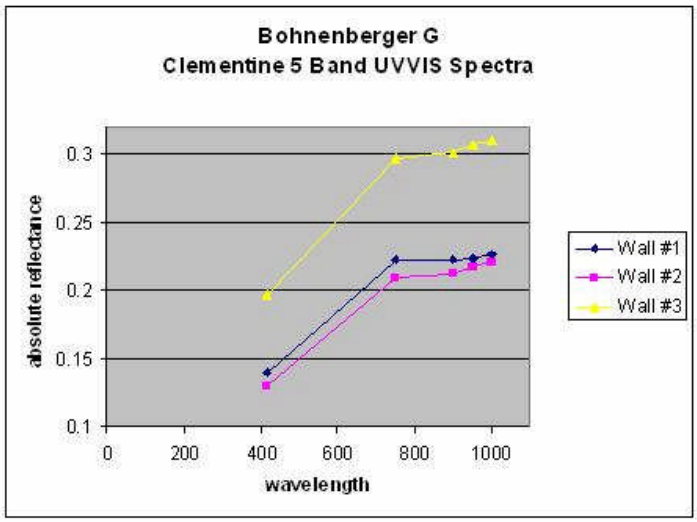

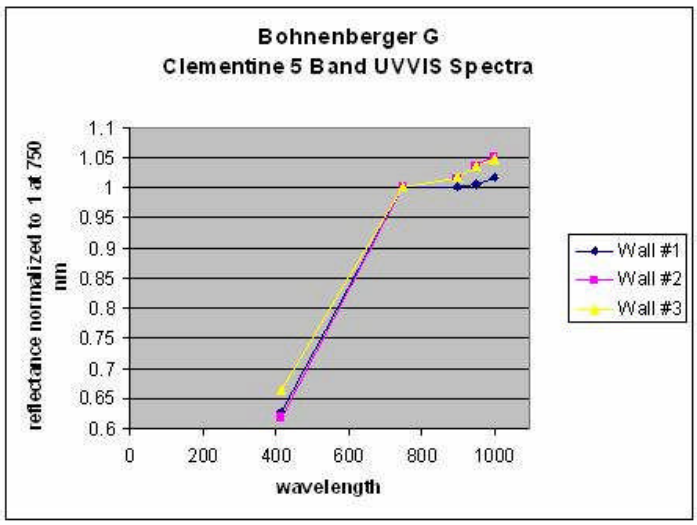

Comparison of Natural Color and Maturation Ratio Images

Figures 5g & 5h

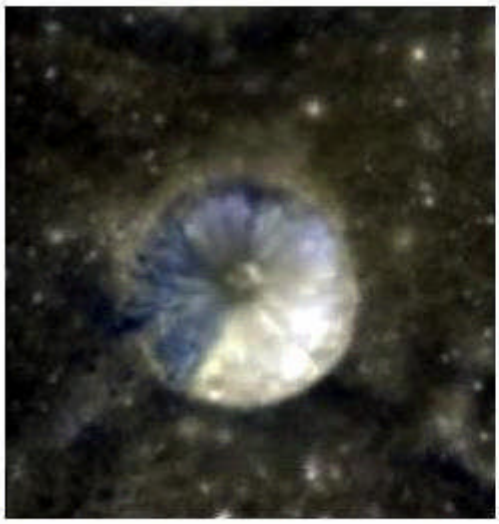

Natural Color

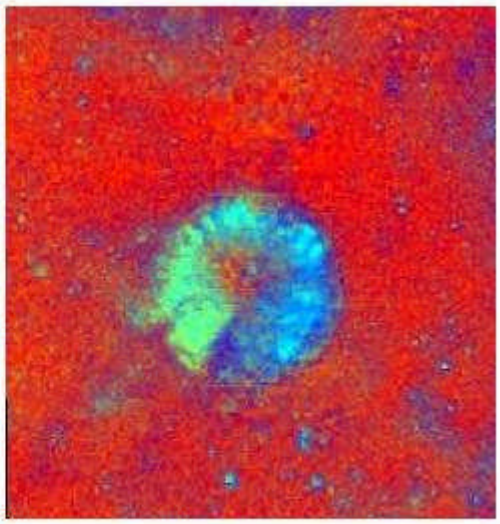

Maturation Ratio

Interpretation Based on Tompkins (1998)

All three wall areas are composed of anorthosite type 2 (An2). The darkest band had an albedo that was 29% less than the lightest band at 750 nm. There is a suggestion in the 7 o'clock to 10 o'clock sector, that the darker albedo wall features seen on the natural color image might correspond to areas of yellow green color on the maturation ratio image possibly indicating a slightly richer iron content than the adjacent lighter bands or the effects of weathering.

6. Theon Senior (Photographic Banded Crater)

Clementine Images with Wall Areas Sampled for Spectra

Figures 6a, 6b, 6c & 6d

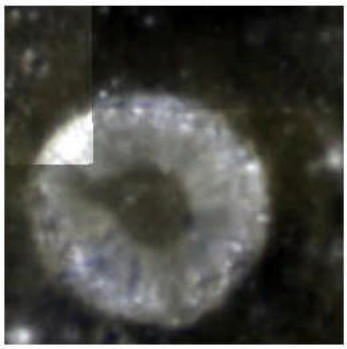

Natural Color

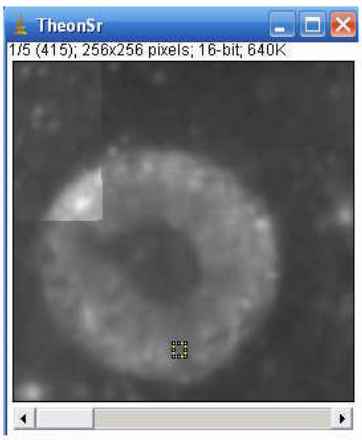

Wall Area #1 (box)

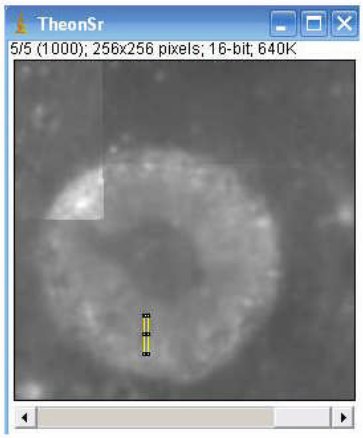

Wall Area #2 (box)

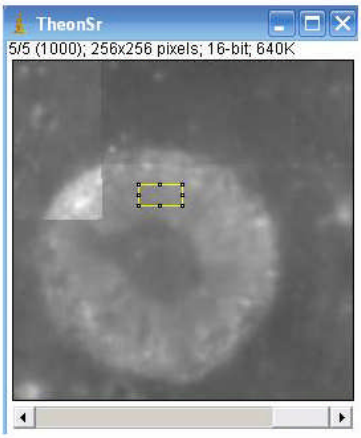

Wall Area #3 (box)

Clementine 5 Band UVVIS Spectra

Figures 6e & 6f

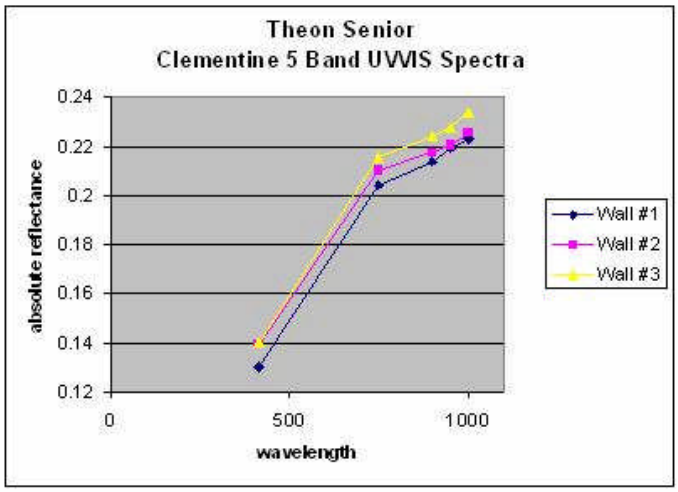

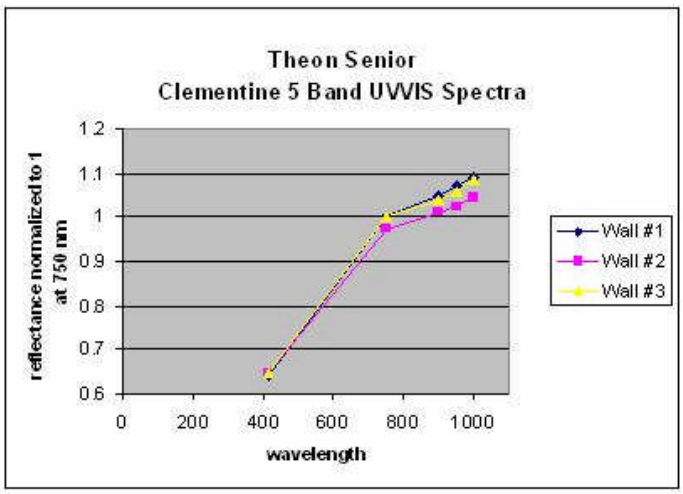

Comparison of Natural Color and Maturation Ratio Images

Figures 6g & 6h

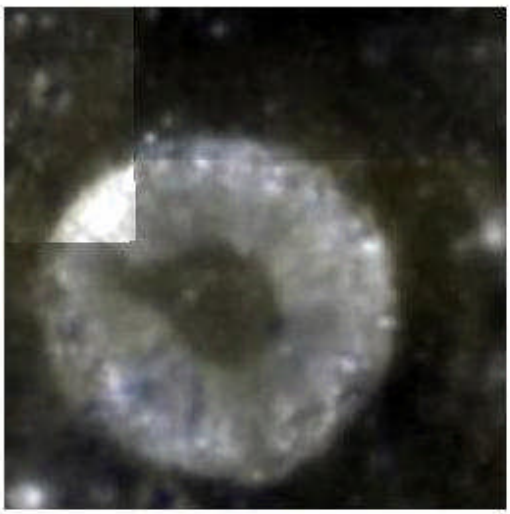

Natural Color

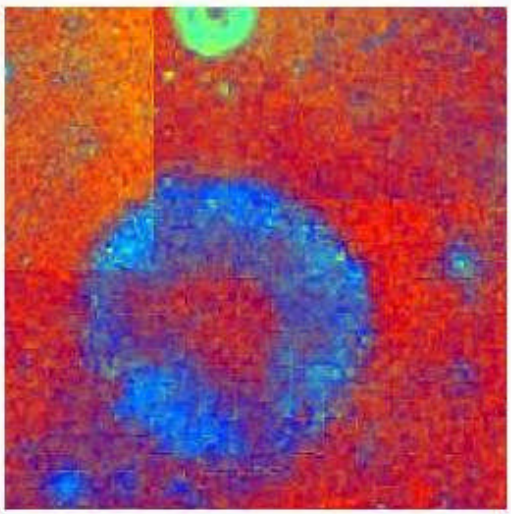

Maturation Ratio

Interpretation from the Method of Tompkins (1998)

All three areas of the wall show spectra consistent with Anorthosite type 1 (An1). The darkest band had an albedo that was 5% less than the lightest band at 750 nm.

7. Aristarchus (Visual and Photographic Banded Crater)

Clementine Images with Wall Areas Sampled for Spectra

Figures 7a, 7b, 7c & 7d

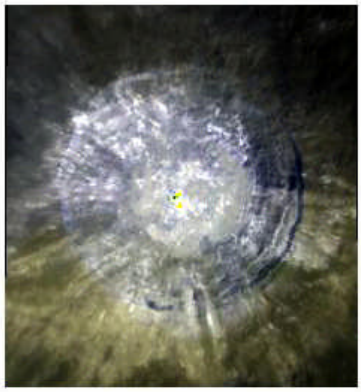

Natural Color

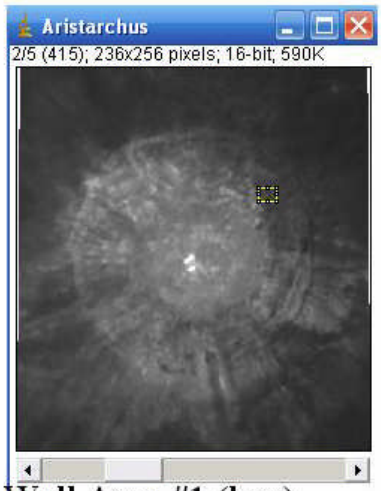

Wall Area #1 (box)

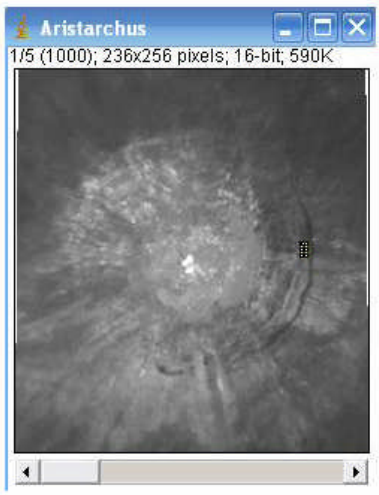

Wall Area #2 (box)

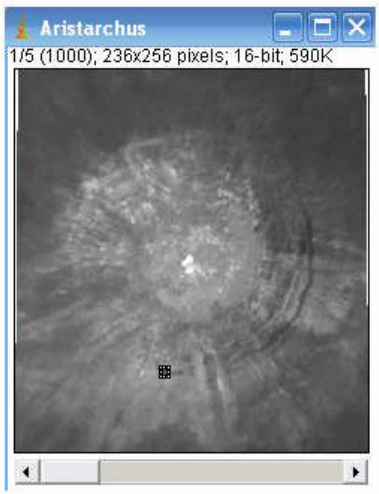

Wall Area #3 (box)

Figures 7e, 7f, 7g & 7h

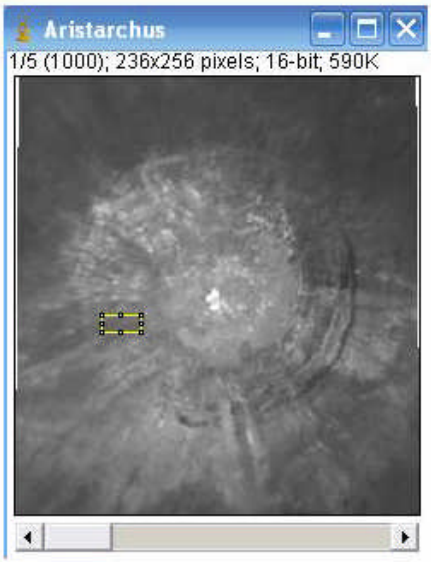

Wall Area #4 (box)

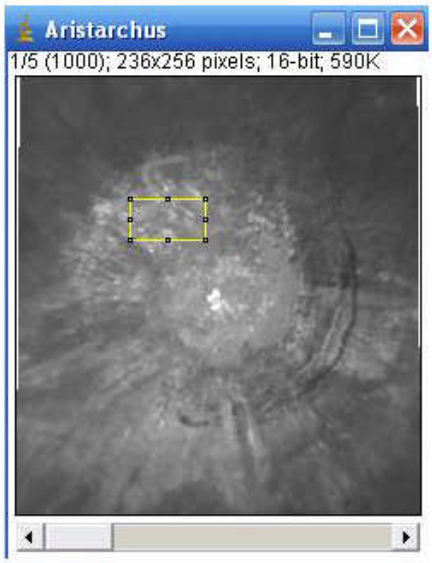

Wall Area #5 (box)

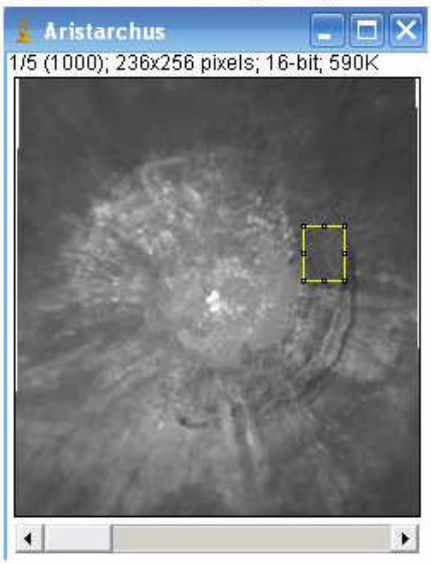

Wall Area #6 (box)

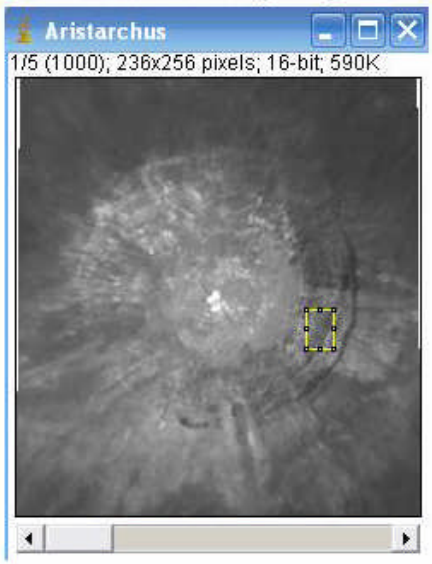

Wall Area #7 (box)

Clementine 5 Band UVVIS Spectra

Figures 7i & 7j

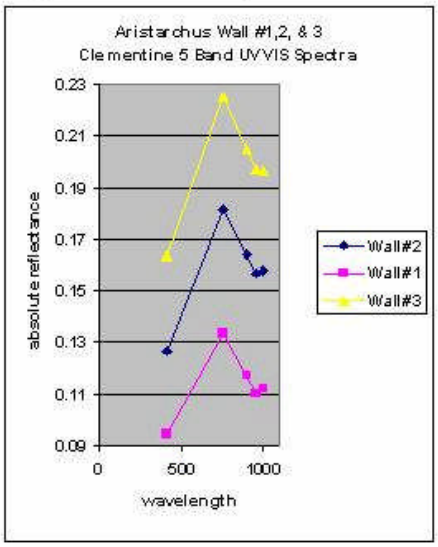

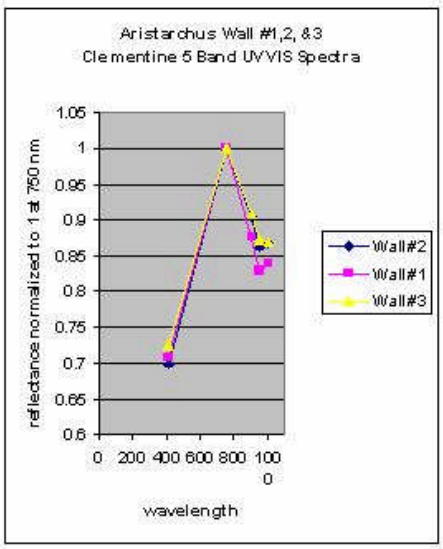

Figures 7k & 7l

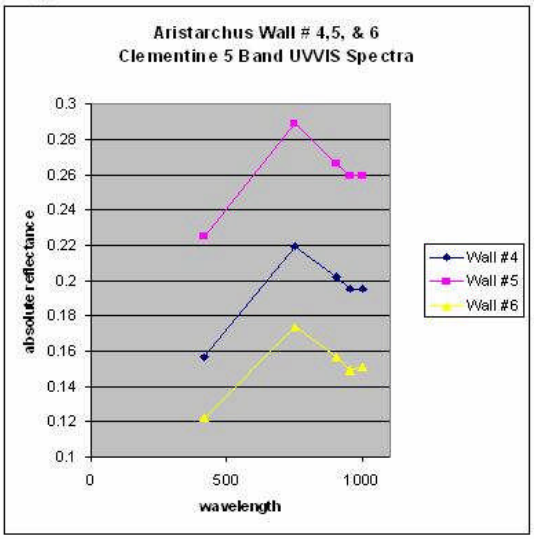

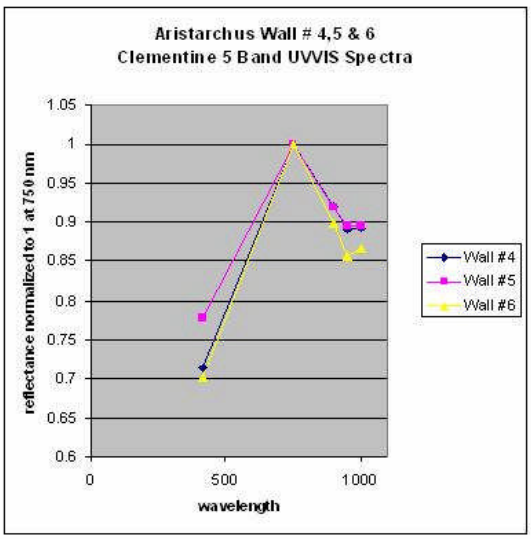

Figures 7m & 7n

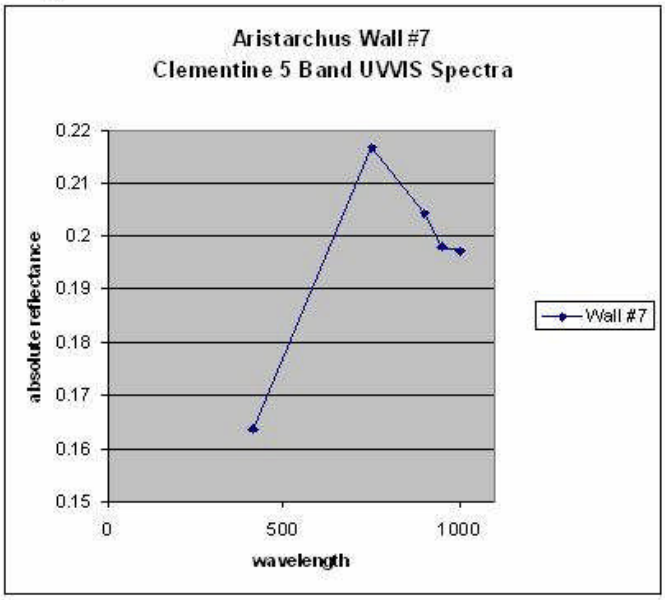

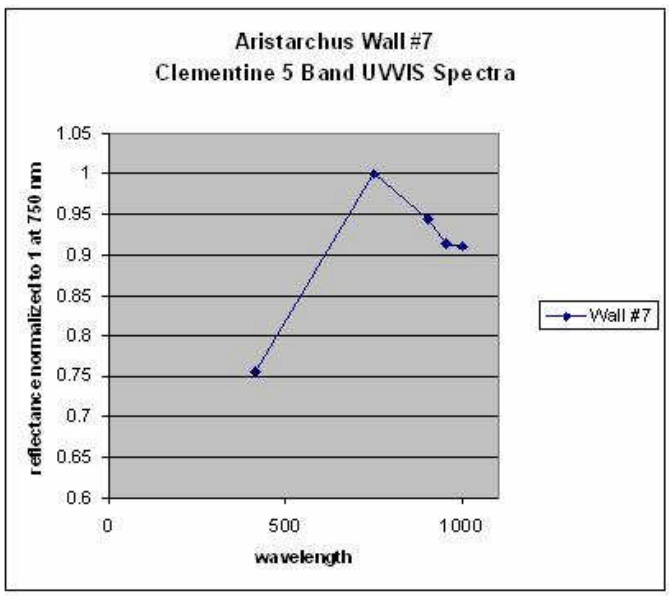

Figures 7o, 7p & 7q

Central Peak Area #1 (box)

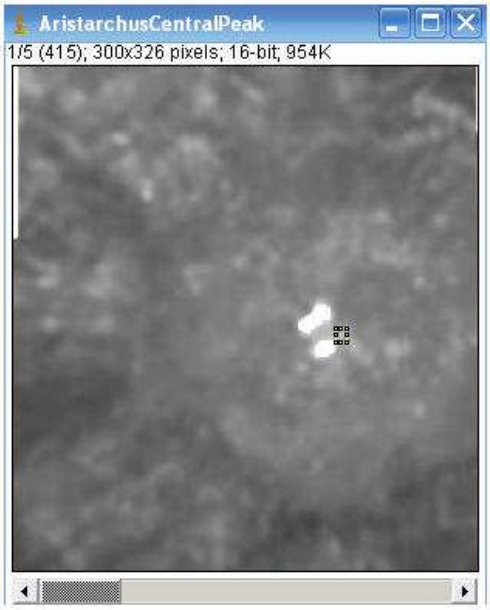

Central Peak Area #2 (box)

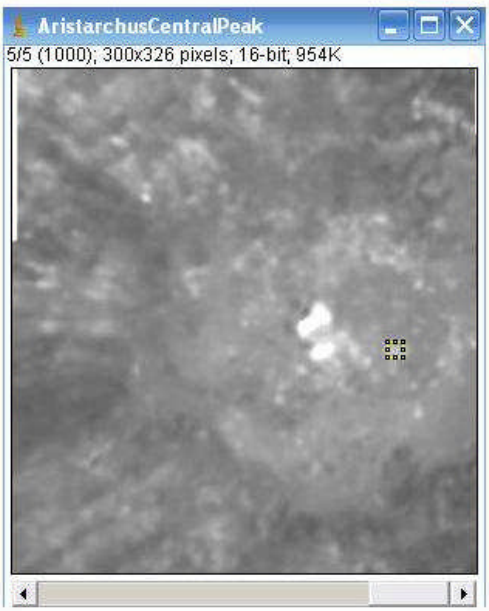

Central Peak Area #3 (box)

Clementine 5 Band UVVIS Spectra

Figures 7r & 7s

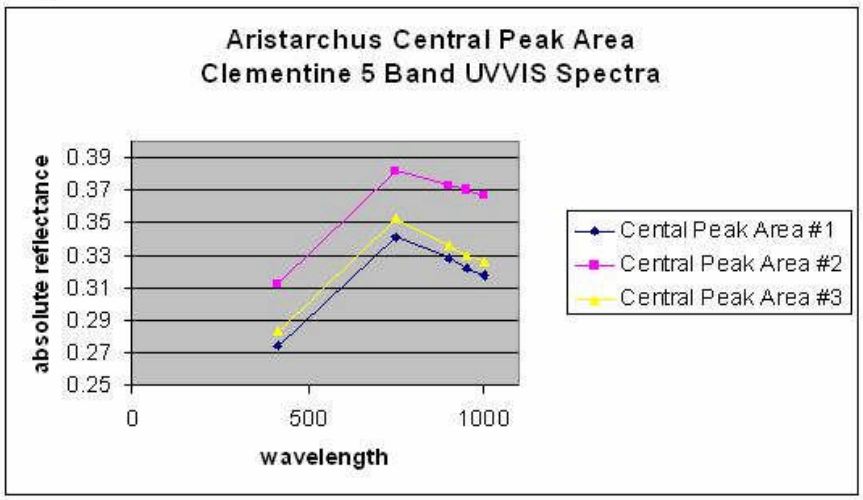

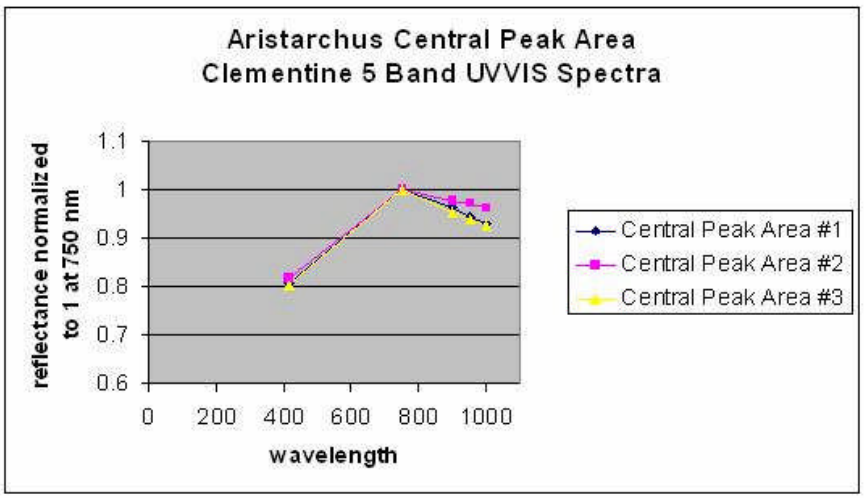

Comparison of Natural Color and Maturation Ratio Images

Figures 7t & 7u

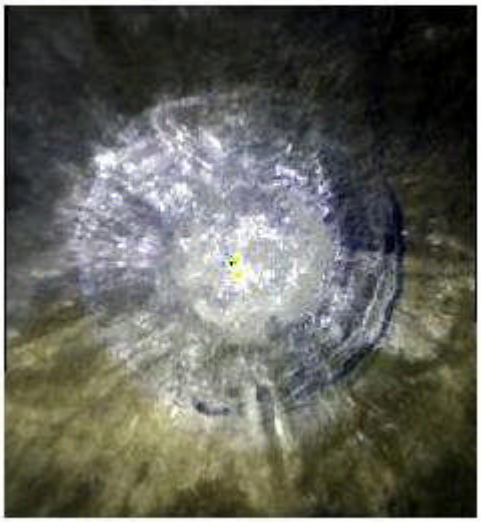

Natural Color

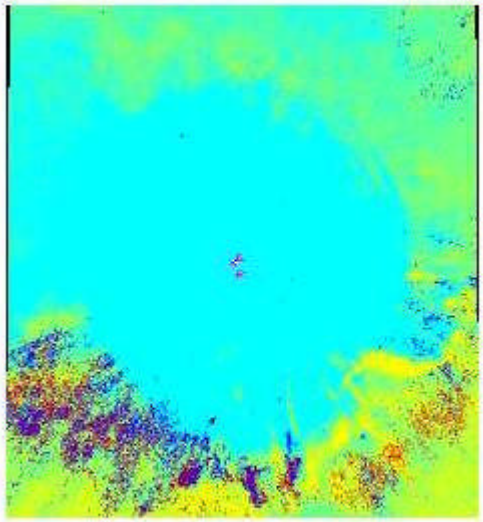

Maturation Ratio

Apollo Hasselblad Camera Images of Aristarchus

Figure 7v and 7w

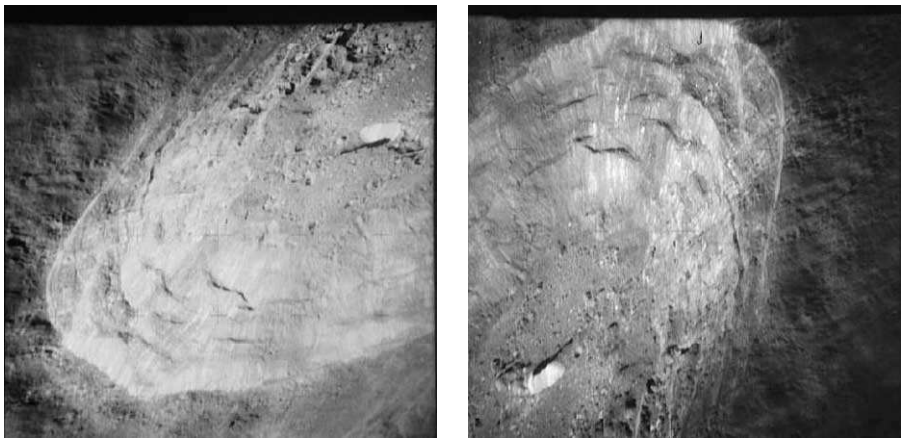

Figure 7x

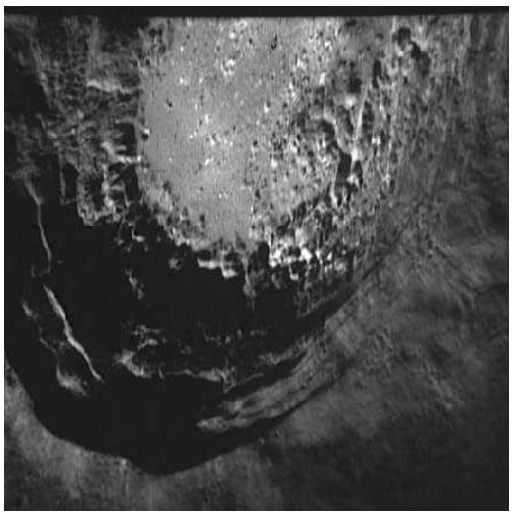

Interpretation from the Method of Tompkins (1998)

Wall areas studied show spectra consistent with Anorthositic gabbro (AG) or Gabbro (G) with the mafic component most likely being a clinopyroxene. The darkest band had an albedo that was 67% less than the lightest band at 750 nm. Although the maturation image is uniformly light blue, the Apollo Hasselblad camera images of the crater raise the possibility of landslide activity and perhaps the banding of the crater has occurred on this basis. It was not possible to measure the spectra of the central peaks themselves because of overexposure of the 415 nm image, but spectra of three adjacent hills/ hummocks were obtained and showed a composition of anorthositic troctolite (AT).

8. Aristillus (Visual Banded Crater)

Clementine Images with Wall Areas Sampled for Spectra

Figures 8a, 8b, 8c & 8d

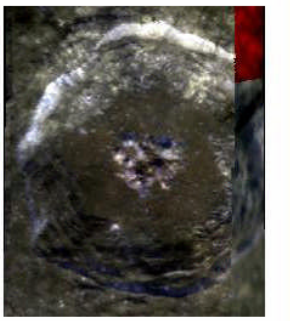

Natural Color

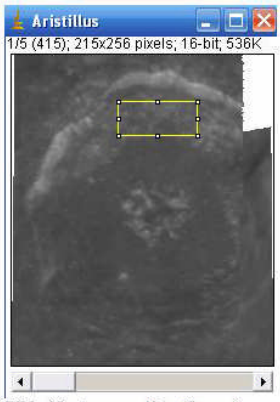

Wall Area #1 (box)

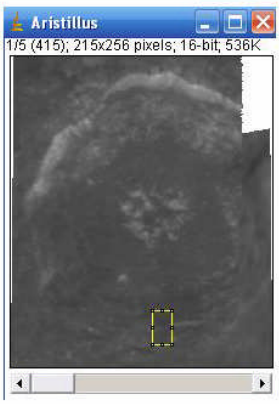

Wall Area #2 (box)

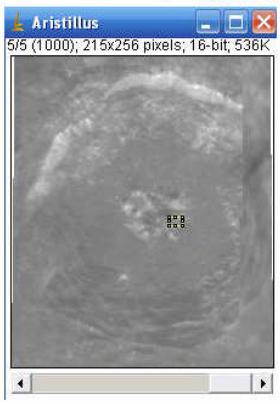

Central Peak Area #1 (box)

Clementine 5 Band UVVIS Spectra:

Figures 8e & 8f

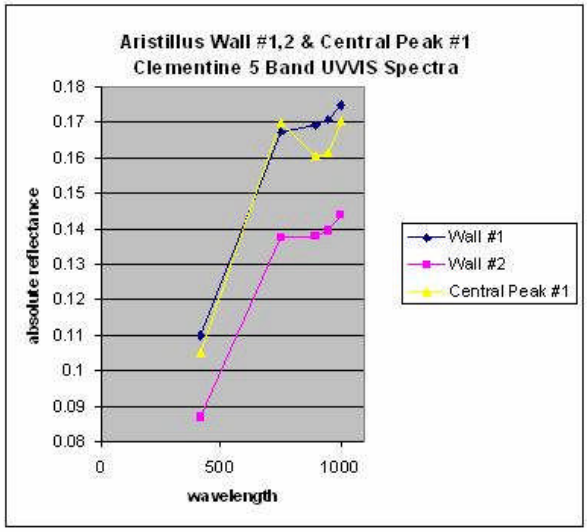

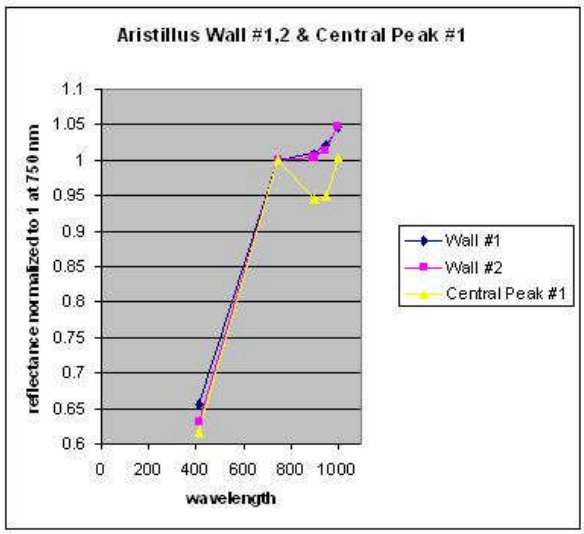

Comparison of Natural Color and Maturation Ratio Images

Figures 8g & 8h

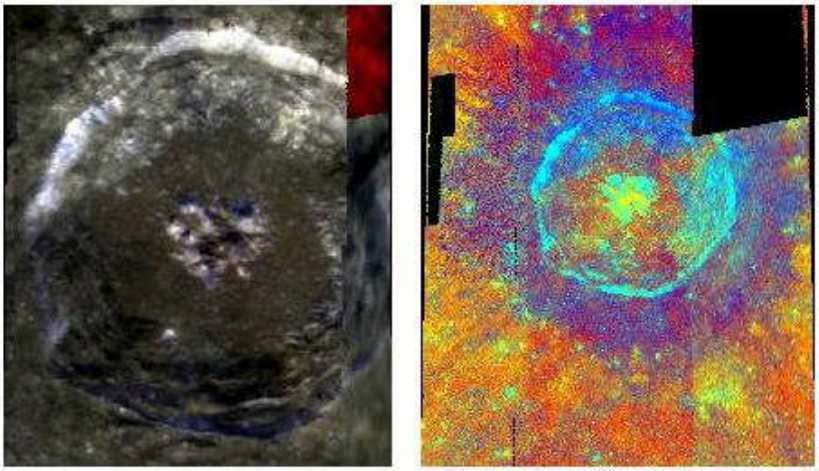

Natural Color Maturation Ratio

Interpretation from the Method of Tompkins (1998)

The crater walls are consistent with being composed of Gabbroic noritic troctolitic anorthosite (GNTA) while the central peak area is consistent with anorthositic norite (AN). The darkest band had an albedo that was 18% less than the lightest band at 750 nm. The lower half of the crater wall, with its relatively darker albedo, appears in a lighter hue of yellowish turquoise on the maturation ratio image.

9. Conon (Visual Banded Crater)

Clementine Images with Wall Areas Sampled for Spectra

Figures 9a, 9b, 9c and 9d

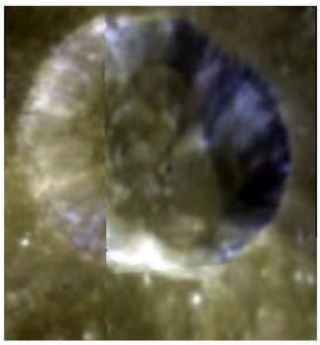

Natural Color

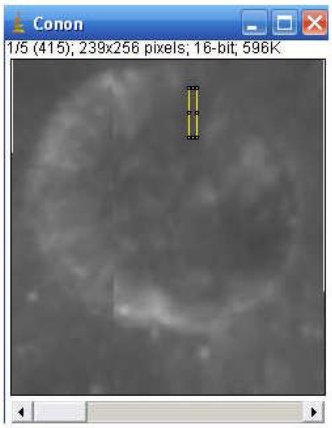

Wall Area #1 (box)

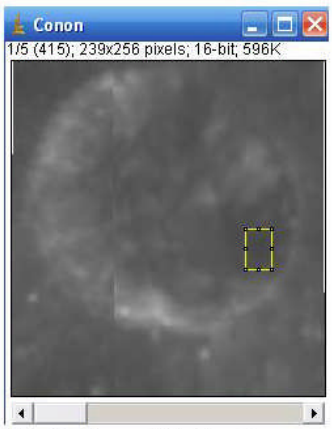

Wall Area #2 (box)

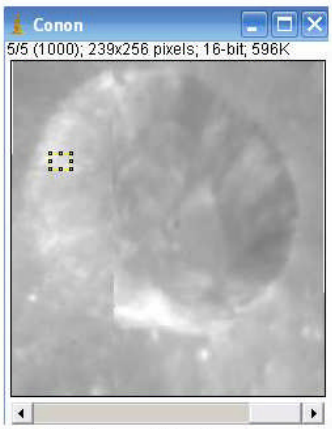

Wall Area #3 (box)

Clementine 5 Band UVVIS Spectra

Figure 9e & 9f

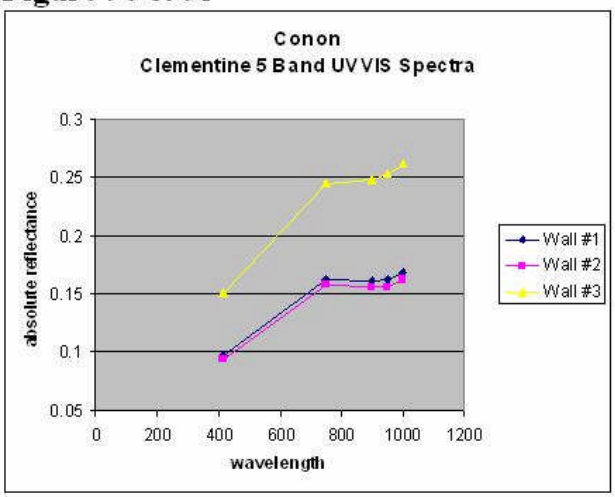

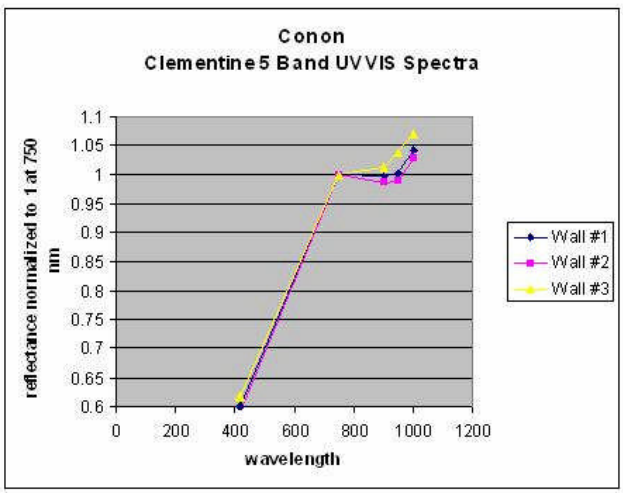

Comparison of Natural Color and Maturation Ratio Images

Figures 9g & 9h

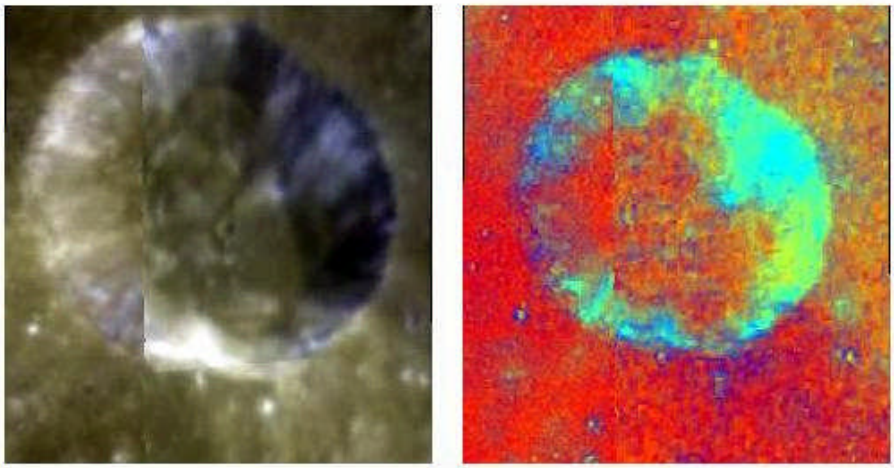

Natural Color Maturation Ratio

Interpretation from the Method of Tompkins (1998)

The crater walls are consistent with being composed of anorthosite (An2) type 2. The darkest band had an albedo that was 35% less than the lightest band at 750 nm. It is again interesting that the crater wall sector from about 1 o'clock to 4 o'clock, with its darker albedo on the natural color image, corresponds to an area of yellowish color on the maturation image. Although it is unclear, perhaps this reflects a slightly higher iron content or effects of weathering.

10. Theatetus (Visual Banded Crater)

Clementine Images with Wall Areas Sampled for Spectra

Figures 10a, 10b & 10c

Natural Color

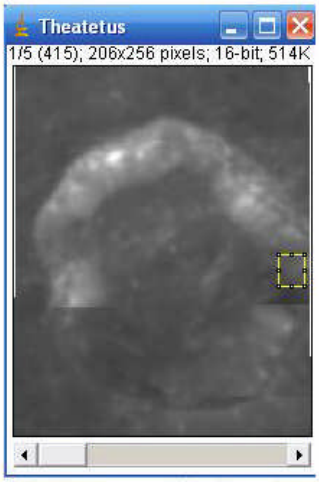

Wall Area #1 (box)

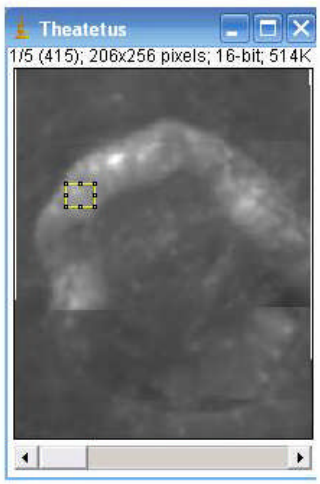

Wall Area #2 (box)

Clementine 5 Band UVVIS Spectra

Figures 10d & 10e

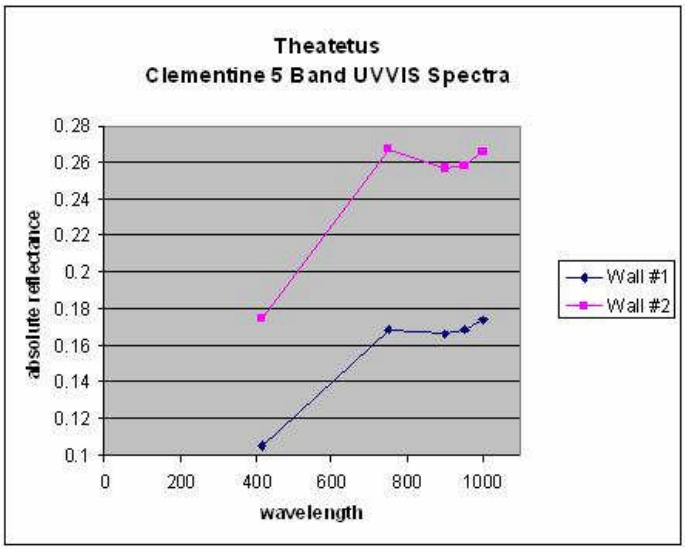

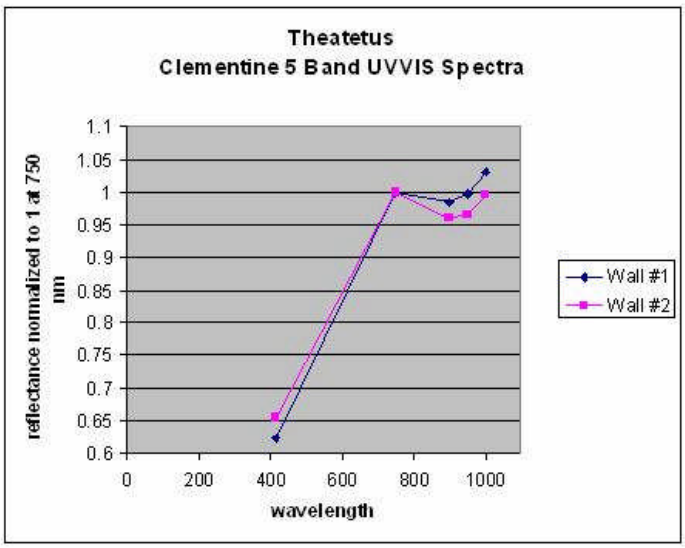

Comparison of Natural Color and Maturation Ratio Images

Figures 10f & 10g

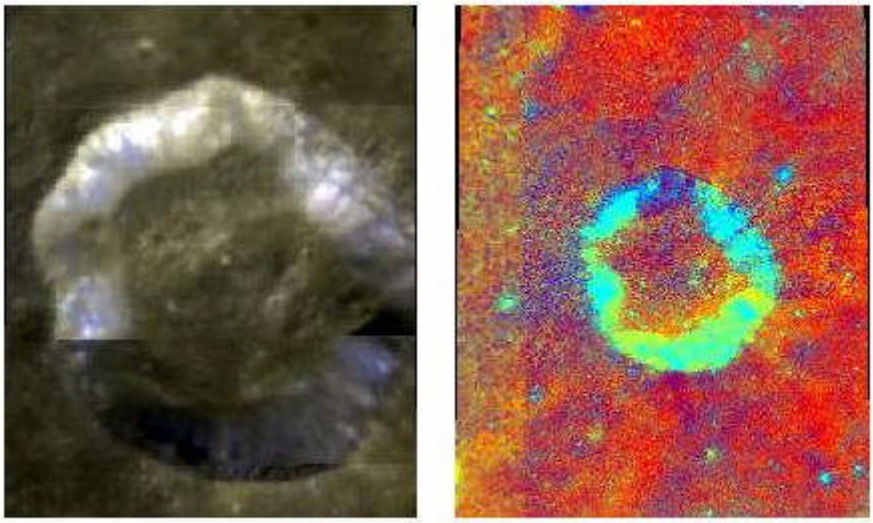

Natural Color Maturation Ratio

Interpretation From Tompkins (1998)

The crater walls are consistent with being composed of gabbroic noritic troctolitic anorthosite (GNTA). The darkest band had an albedo that was 37% less than the lightest band at 750 nm. The lower half of the crater wall has a darker albedo and seems to correspond with areas of yellowish color on the maturation image which may incidate a slightly higher iron content.

11. Brayley (Visual Banded Crater)

Figures 11a, 11b, 11c & 11d

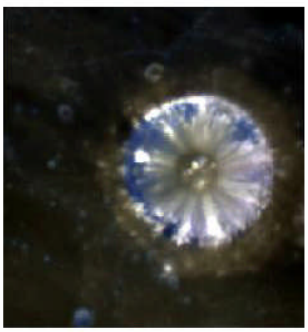

Natural Color

Wall Area #1 (box)

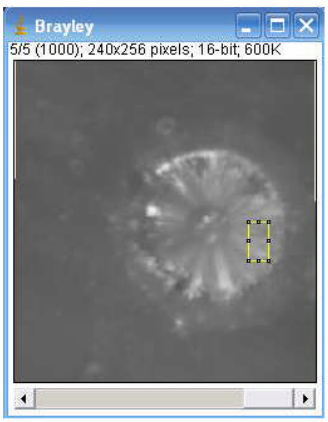

Wall Area #2 (box)

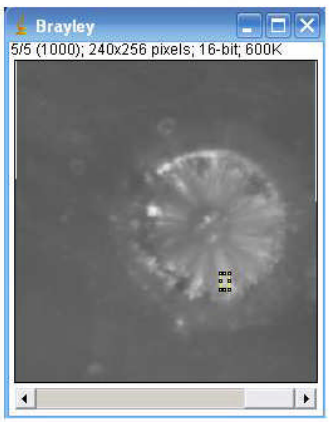

Wall Area #3 (box)

Clementine 5 Band UVVIS Spectra

Figures 11e & 11f

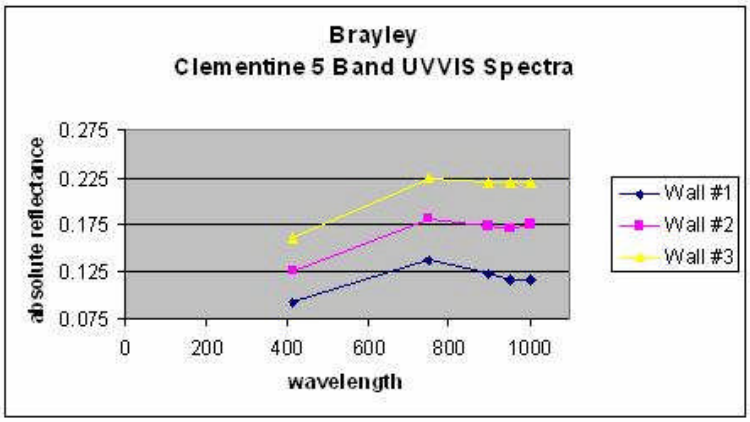

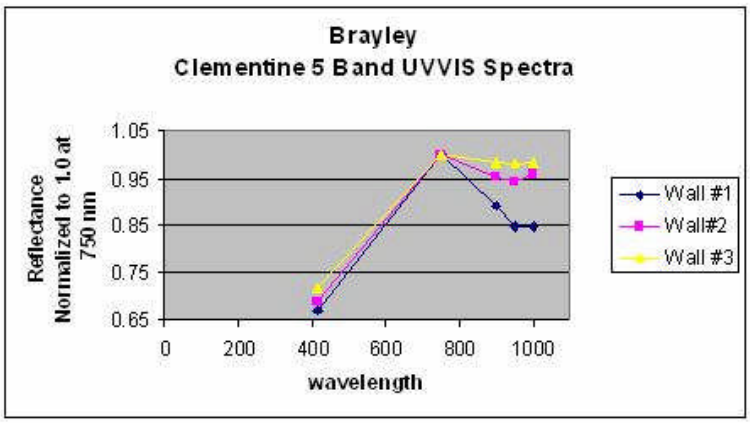

Comparison of Natural Color and Maturation Images

Figures 11g & 11h

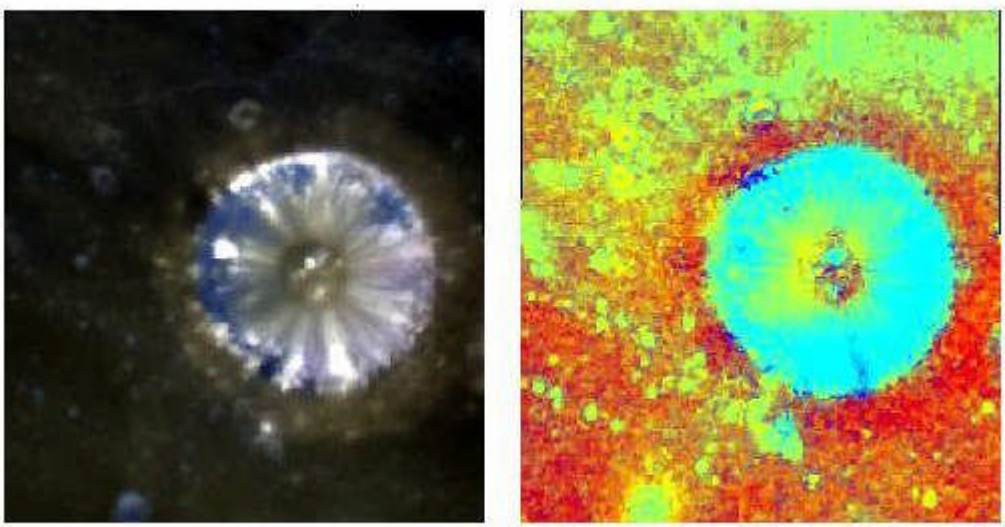

Natural Color Maturation Ratio

Interpretation Based on Tompkins (1998)

The darkest bands are composed of anorthositic gabbro consistent with a basaltic component while the lightest are composed of anorthosite type 2 (An2) and anorthositic norite (AN). The albedo difference between darkest and lightest bands is 39 percent. This crater was recently discussed in the LPOD series by Charles Wood (see http://www.lpod.org/?p=1659) who felt that the lighter bands were the result of landslides exposing fresher material with the albedo of adjacent darker bands influenced by the effects of longer term weathering. Comparison of natural color and maturation images shows that darker albedo areas on the former probably correspond to areas of yellowish color on the latter. This may indicate areas of slightly higher iron content or effects of weathering.

Discussion

With the exception of Schomberger A, light and dark bands could be distinguished on Clementine color albedo images in each of the craters analyzed with dark bands typically having an indigo to purplish hue. Of the eleven craters analyzed light and dark bands were composed of the same material in nine. Of these nine crater walls, four were composed of anorthosite type 2 (An2), two were composed of anorthositic norite (AN), two were composed of gabbroic noritic troctolitic anorthosite (GNTA), and one was composed of anorthosite type 1 (An1). Two craters, Aristarchus and Brayley, had heterogenous walls with more than one composition present. In the case of Brayley, anorthosite type 2 (An2), anorthositic norite, and anorthositic gabbro due to basaltic contamination were present. In the case of Aristarchus most wall areas studied showed a composition of either anorthositic gabbro or gabbro with the mafic component being a clinopyroxene. Analyzed in terms of absolute reflectance, dark bands did show a significantly lower albedo than light bands. The albedo difference was greatest for craters described as visual banded craters in the original catalog by Albineri and Lenham, with craters designated as photographic banded craters typically showing smaller albedo differences. It is interesting that when the natural color images and maturation ratio images are compared for these craters, a frequent finding is that areas of indigo or purplish darkening of the wall on the natural color images often corresponded to areas of yellowish or yellowish green on the maturation image. This may indicate that such terrain has a slightly higher iron content. However, since the mafic composition of dark and light bands usually appeared quite similar (with Brayley and only one wall area studied in Aristarchus being exceptions), perhaps this apparent increase in iron content is an effect of weathering. This might favor landslides as a possible mechanism of band formation whereby adjacent sectors of a crater wall show albedo differences based on creation of freshly exposed surfaces. Freshly exposed sectors would be expected to appear more immature on maturation ratio images than adjacent areas whose surface materials have been exposed to weathering for a longer period of time. The crater list is most likely incomplete and craters such as Dionysius could well be included (Appendix 3). The impact that created Dionysius is particularly interesting in that, like Brayley, it appears to have penetrated a shallow subsurface basalt layer and banding in the crater wall has anorthositic areas but also sectors with significant amounts of norite and basalt. Clementine data could likely be utilized to substantially expand the existing list of banded craters.

References

[1] Tompkins, S. (1998) Mafic Plutons in the Lunar Highland Crust. LPSC XXIX p. 999-1000.

[2] Albineri, KW and Lenham, AP (1955) Lunar Banded Craters. Journal of the British Astronomical Association. March Issue.

[3]Tompkins, S and Pieters, CM (1997) Composition of the Lunar Crust Beneath the Megaregolith, LPSC XXVIII, LPI, Houston, TX 1439-1440.

[4]Le Mouelic S; Langevin Y; Erard S (1999). Discrimination between Olivine and Pyroxene from Clementine NIR data: Application to Aristarchus Crater. LPSC XXX

[5] Chevrel SD, Pinet PC, et al. (2004) Composition and Structural Study of the Aristarchus Plateau from Integrated UV-VIS-NIR Spectral Data. Lunar and Planetary Science XXXV.

[6] Pieters, CM and Englert PAJ: Topics in Remote Sensing 4: Remote Geochemical Analysis: Elemental and Mineralogical Composition. Chapter 14: Compositional Diversity and Stratigraphy of the Lunar Crust Derived from Reflectance Spectroscopy. pp. 309-342. Cambridge University Press 1993 (ISBN: 0-521-40281-6).

Table 1

Crater	% Albedo Difference Between Dark & Light Bands	Cataloged as Visual or Photographic Banded Crater by
Adams B	39	Photographic
Aristarchus	67	Visual
Aristillus	18	Visual
Bohenberger G	29	Photographic
Brayley	39	Visual
Cichus C	9	Photographic
Conon	35	Visual
Davy A	39	Photographic
Schomberger A	50	Visual
Theatetus	37	Visual
Theon Senior	5	Photographic

Appendix 1

Compilation of Lunar Banded Craters

Courtesy of

William Dembowski, ALPO

http://www.zone-vx.com/alpo-bcp-longlist.pdf

(Modified From Original Compilation by Albineri & Lenham, JBAA 1955)

BANDED CRATERS BY NAMED FEATURE

NAMED FEATURE	LUNAR LONG.	LUNAR LAT.	GROUP
(Unnamed Feature)	E0.9	S18.0	1
(Unnamed Feature)	E4.8	N23.4	4
(Unnamed Feature)	W45.4	S23.6	3
(Unnamed Feature)	E56.6	N38.3	1
Abbot (Apollonius K)	E54.8	N5.6	1
Abenezra A (Mayfair A)	E10.5	22.8S	2
Abenezra B	E10.1	S20.8	4
Abulfeda A	E10.8	S16.4	1
Abulfeda F	E13.0	S16.2	2
Abulfeda M	E12.2	S15.1	4
Adams B	E65.6	S31.5	2
Agatharchides A (Moore)	W28.4	S23.2	5
Airy A	E7.7	S17.0	4
Albategnius L	E6.3	S12.1	1
Almanon C	E16.0	S16.1	4
Alpetragius B (Garcia-Gomez)	W6.8	S15.1	4
Ammonius (Ptolemaeus A)	W0.8	S8.5	4
Anaxagoras	W10.1	N73.4	N/A
Apollonius B	E57.6	N5.7	1
Apollonius L	E54.6	N6.5	1
Argelander	E5.8	S16.5	4
Argelander A	E6.8	S16.5	4
Aristarchus	W47.4	N23.7	1
Aristillus	E1.2	N33.9	3
Asada (Taruntius A)	E7.3	N49.9	4
Atlas A	E49.6	N45.3	1
Barocius M	E19.5	S42.2	1
Bayer N	W29.2	S48.3	2
Beaumont A	E27.7	S16.3	N/A
Beaumont D	E26.2	S17.0	4
Beaumont E	E27.5	S18.8	1
Bessarion	W37.3	N14.9	N/A
Biot	E51.1	S22.6	1
Biot A	E48.9	S22.2	1
Birt	W8.5	S22.4	4
Black (Kastner F)	E80.4	S9.2	1
Bode	W2.4	N6.7	1
Bode A	W1.1	N9.0	1
BodeB	W3.1	N8.7	4
Boguslawsky C	E27.7	S70.9	1
Bohnenberger G	E41.9	S17.2	1
Bombelli (Apollonius T)	E56.2	N5.3	4
Born (Maclaurin Y)	E66.8	S6.0	1
Boussingault D	E44.9	S63.5	2
Brayley	W36.9	N20.9	N/A
Burg	E28.2	N45.0	N/A
Busching E	E18.4	S36.6	1
Byrgius B	W60.8	S23.9	1
Campanus A	W28.6	S26.0	1

NAMED FEATURE	LUNAR LONG.	LUNAR LAT.	GROUP
Capuanus L	W26.3	S38.3	1
Cavendish E	W54.2	S25.4	3
Cayley	E15.1	N4.0	1
Cepheus A	E46.5	N41.0	4
Chladni	E1.1	N4.0	4
Cichus B	W19.3	S33.2	1
Cichus C	W21.8	S33.5	4
Clavius G	W13.9	S52.0	2
Cleomedes A	E55.0	N28.9	4
Conon	E2.2	N21.6	2
Crile (Proclus F)	E46.0	N14.2	4
Cuvier B	E13.8	S51.7	2
Cuvier E	E12.9	S52.3	2
Cyrillus F	E25.5	S15.3	2
Darney (Lubiniezky B)	W23.5	S14.5	4
Davy A	W7.7	S12.2	4
Davy G	W5.1	S10.4	1
Dawes	E26.4	N17.2	N/A
Descartes A	E15.2	S12.1	4
Drebbel B	W47.3	S37.8	2
Drebbel F	W44.6	S42.7	2
Drebbel G	W45.2	S43.9	2
Drebbel J	W52.3	S40.6	1
Epimenides A	W30.1	S43.2	2
Eudoxus A	E20.0	N45.8	4
Fabbroni (Vitruvius E)	E29.2	N18.7	1
Fourier E	W50.1	S28.7	1
Fra Mauro A	W20.9	S5.4	4
Fra Mauro B	W21.7	S4.0	4
Fracastorius A	E36.5	S24.4	1
Fracastorius B	E37.2	S22.5	2
Fracastorius N	E34.0	S23.2	1
Fracastorius T	E37.4	S19.8	2
Franck (Romer K)	E35.5	N22.6	1
G. Bond	E36.2	N32.4	1
Gambart A	W18.7	N1.0	4
Gambart B	W11.5	N2.2	4
Gambart C	W11.8	N3.3	4
Gemma Frisius Ea	E11.4	S35.2	4
Gemma Frisius Eb	E11.9	S36.7	N/A
Gemma Frisius K	E11.0	S37.4	4
Glaisher	E49.5	N13.2	4
Guericke B	W15.3	S14.5	2
Guericke E	W12.0	S9.6	1
Gutenberg A	E39.9	S9.0	1
Haidinger	W25.0	S39.2	2
Haidinger J	W24.4	S37.9	N/A
Hainzel B	W33.4	S38.0	2
Hainzel J	W37.7	S37.8	1
Hainzel K	W32.3	S37.5	1
Hainzel R	W36.4	S38.7	1

NAMED FEATURE	LUNAR LONG.	LUNAR LAT.	GROUP
Henry Freres (Prosper Henry)	W58.9	S23.5	2
Hercules C	E35.3	N42.7	1
Hercules D	E39.7	N44.8	1
Hercules G	E39.2	N46.4	4
Herschel C	W2.1	S5.7	4
Hippalus B	W30.0	S25.1	4
Hipparchus K	E2.2	S6.9	1
Isidorus D	E34.1	S4.2	1
Isidorus E	E32.6	S5.3	1
Jacobi J	E10.3	S58.0	4
Janssen	E34.4	S44.9	1
Kaiser C	E9.7	S35.6	1
Kepler	W38.0	N8.1	2
KiesA	W22.7	S28.3	3
Kircher A	W42.1	S66.1	2
Konig	W24.6	S24.1	2
Lalande A	W9.8	S6.6	4
Lalande C	W6.9	S5.6	4
Langrenus G	E65.4	S12.1	4
Langrenus M	E66.4	S9.8	4
Lansberg B	W28.1	S2.5	4
Lansberg D	W30.6	S3.0	N/A
Lassell D	W10.5	S14.5	4
Lee E (Vitello C)	W42.5	S32.4	2
Littrow D	E32.8	N23.7	1
Luther	E24.1	N33.2	1
Maginus P	W11.8	S50.7	N/A
Marco Polo	W2.0	N15.4	4
Marinus A	E73.2	S39.9	2
Mason C	E33.8	N42.9	1
Maury	E39.6	N37.1	4
MeeC	W28.7	S45.3	1
MeeP	W30.0	S45.9	2
Menelaus	E16.0	N16.3	2
Mersenius S	W46.9	S19.2	1
Messala A	E53.8	N36.6	5
Messier	E47.6	S1.9	3
Messier A	E47.0	S2.0	3
Milichius	W30.2	N10.0	N/A
Mosting A	W5.2	S3.2	2
Nicollet	W21.9	S12.5	4
Noggerath J	W47.9	S48.4	2
Opelt E	W17.8	S17.0	4
Palisa C	W6.4	S7.7	4
Palisa D	W6.9	S8.6	4
Palisa T	W8.2	S8.2	1
Palisa W	W6.3	S9.1	N/A
Piccolomini E	E31.8	S26.1	3
Piccolomini G	E34.7	S27.2	3
Piccolomini Q	E36.4	S30.8	1
Piccolomini X	E31.5	S26.9	1

NAMED FEATURE	LUNAR LONG.	LUNAR LAT.	GROUP
Poisson C	E8.6	S33.1	2
Poisson K	E9.6	S32.7	N/A
Polybius A	E28.0	S23.0	N/A
Polybius B	E25.5	S25.5	1
Pons F	E21.2	S23.7	1
Pontanus S	E16.8	S31.4	1
Proclus	E46.8	N16.1	N/A
Proclus A	E42.3	N13.4	4
Proclus D	E41.0	N17.5	1
Proclus G	E42.7	N12.7	4
Proclus J	E44.0	N17.1	4
Pytheas	W20.6	N20.5	2
Rabbi Levi F	E20.5	S36.0	1
Rabbi Levi R	E28.2	S33.6	1
Reichenbach A	E49.0	S28.3	2
Reichenbach C	E43.9	S29.3	2
Reichenbach K	E42.4	S28.8	1
Reichenbach P	E49.9	S32.0	1
Riccius B	E27.8	S37.5	2
Riccius E	E26.4	S39.9	1
Riccius M	E26.4	S37.8	1
Rosse	E35..0	S17.9	1
Sacrobosco C	E15.8	S23.0	1
Schickard L	W59.6	S44.1	1
Schomberger A	E24.9	S78.8	1
Shuckburgh C	E52.7	N43.5	1
Silberschlag	E12.5	N6.2	1
Strabo	E54.3	N61.9	1
Street	W13.3	S46.5	3
Thaetetus	E6.0	N37.0	2
Thebit A	W4.9	S21.5	4
Theon Junior	E15.8	S2.3	1
Theon Senior	E15.4	S0.8	1
Timocharis	W13.1	N26.7	2
Turner	W13.2	S1.4	1
Vitello A	W41.9	S34.1	2
Vitello D	W41.0	S33.2	2
Wilhelm A	W22.0	S44.6	2
Wilhelm B	W22.8	S43.5	2
Wilhelm E	W17.9	S44.1	N/A
Wilhelm K	W21.7	S44.1	3
Wilhelm O	W17.2	S43.1	1
Wilkins A	E18.9	S29.1	1
Zagut A	E21.8	S32.0	1

Appendix 2:

Graphic from Tompkins (1998): Figure AP2-1

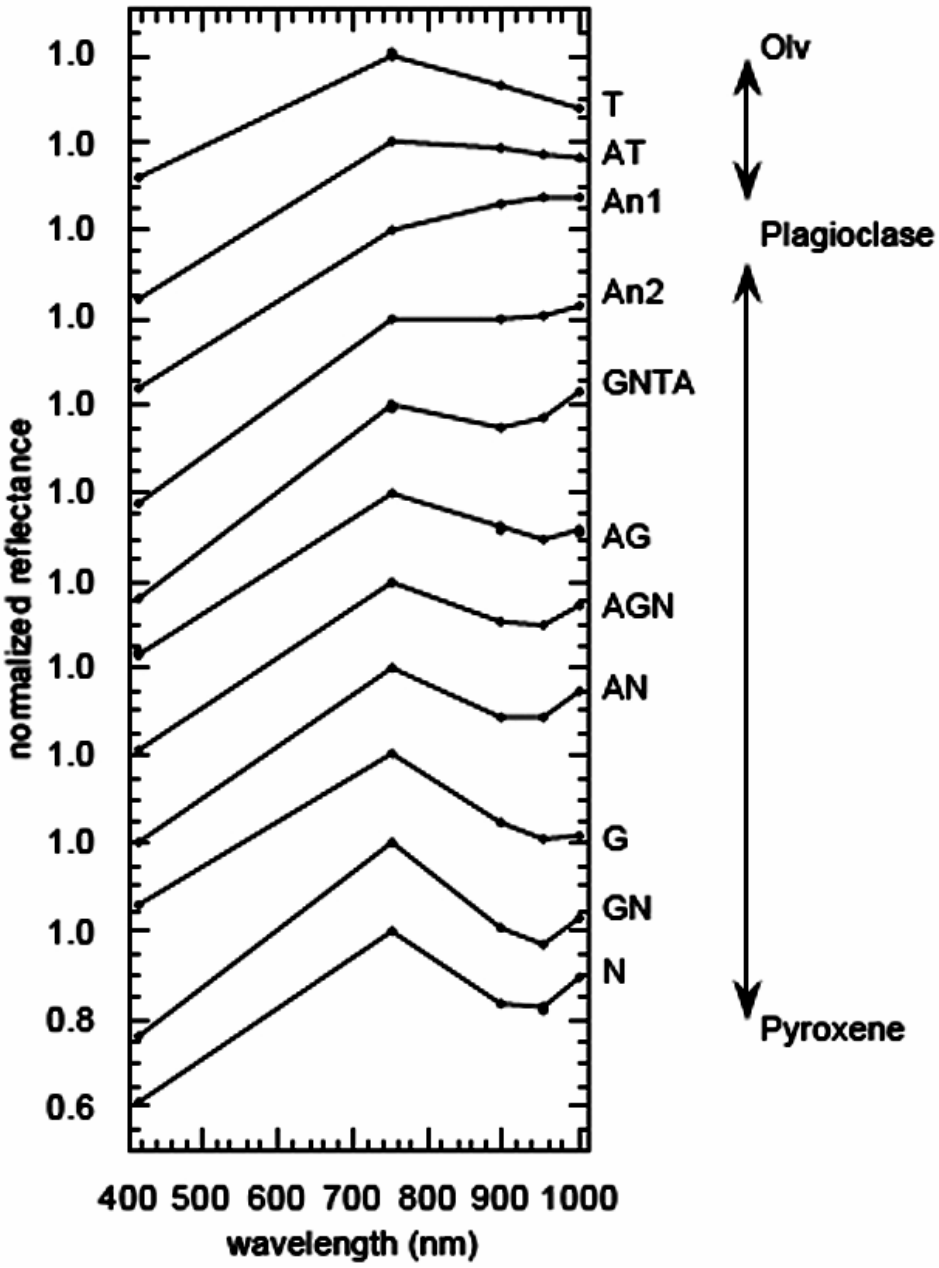

T	**Troctolite**
AT	**Anorthositic Troctolite**
An1	**Anorthosite type 1**
An2	**Anorthosite type 2**
GNTA	**Gabbroic noritic troctolitic anorthosite**
AG	**Anorthositic Gabbro**
AGN	**Anorthositic gabbronorite**
AN	**Anorthositic norite**
G	**Gabbro**
GN	**Gabbronorite**
N	**Norite**

Graphic from Tompkins & Pieters (1997): Figure AP2-2

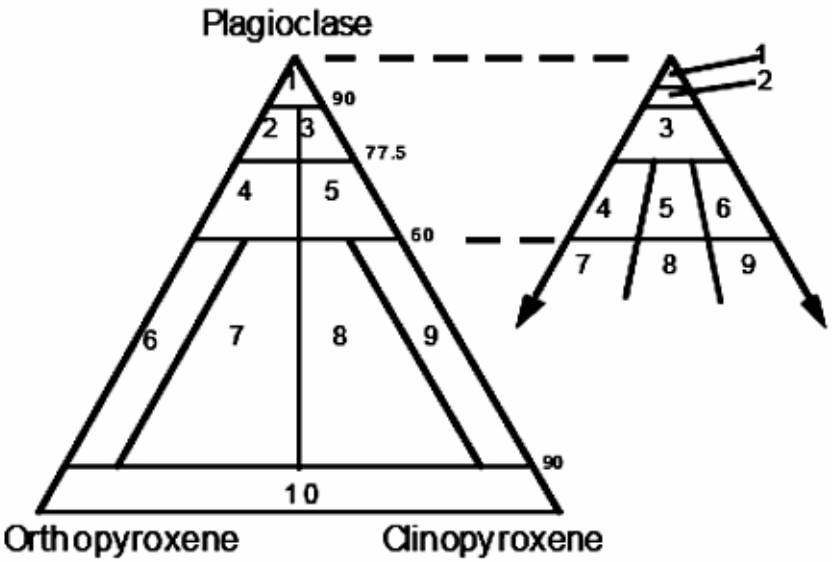

Classification Schemes

Highland Rocks

1 Anorthosite
2 Noritic Anorthosite
3 Gabbroic Anorthosite
4 Anorthositic Norite
5 Anorthositic Gabbro
6 Norite
7 Gabbroic Norite
8 Noritic Gabbro
9 Gabbro
10 Pyroxenite

Clementine Spectra

1 An1 (Anorthosite)
2 An2 (Anorthosite)
3 GNTA (Mafic+Anorthosite)
4 AN (Anorthositic Norite)
5 AGN (Anorthositic Gabbronorite)
6 AN (Anorthositic Norite)
7 N (Norite)
8 GN (Gabbronorite)

Appendix 3:

Significant Banded Craters not in the Albineri & Lenham 1955 catalog

Example: Dionysius

Figure AP3-1 and AP3-2

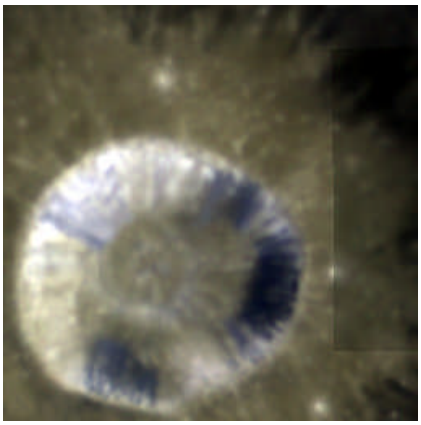

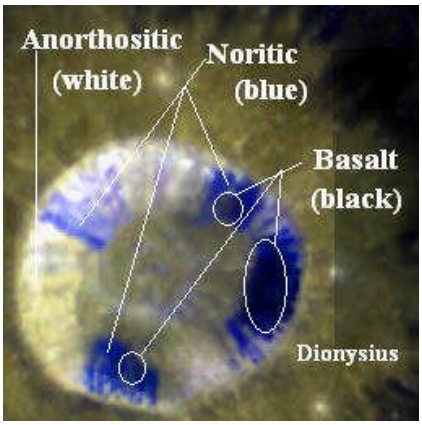

Clementine Natural Color

Figure AP3-3

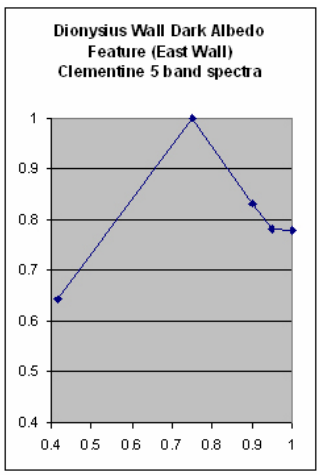

Normalized Reflectance

Figure AP3-4

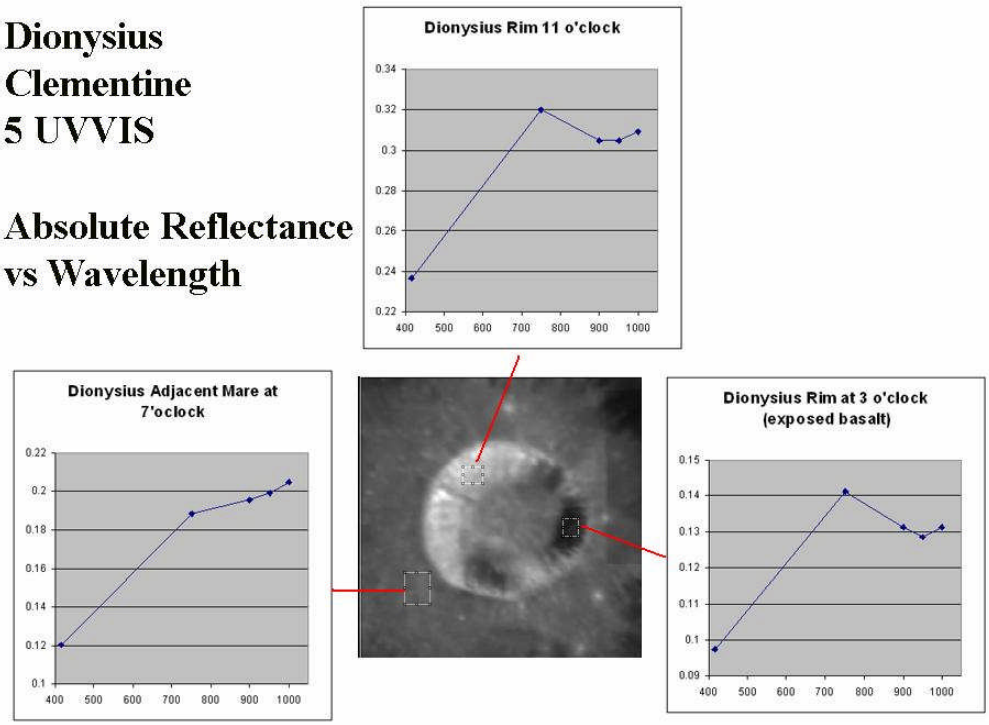
Dionysius
Clementine
5 UVVIS
Absolute Reflectance
vs Wavelength
Dionysius Rim 11 o'clock
Dionysius Adjacent Mare at 7'oclock
Dionysius Rim at 3 o'clock (exposed basalt)

Detection of satellites and space debris in transit across the moon

By Raffaello Lena

Geologic Lunar Research (GLR) group

Abstract

Glints off of satellites and space debris can be identified by their motion during the acquired frames and for the periodicity of their light curves. This paper describes an object in transit across the moon. The space debris FENGYUN 1C DEB (1999-025-AHJ) is more plausible source for the detected trailed flashes. The current techniques and methodologies for acquisition of the AVIs film and identification of the satellites in transit across the moon are presented.

1. Origin and interpretation of detected flashes

Lunar flashes can be caused spuriously by a number of factors including camera noise, cosmic rays, glints coming from space debris and satellites, and terrestrial meteorites with trajectories toward the observer. The possibility that a recorded flash is due to camera noise or a cosmic ray can be eliminated by either slightly defocusing the image to be recorded, or by using a Hartmann mask (cf. Lena and Evans, 2008; Lena, 2002). Cosmic rays and camera noise produce single pixel aberrations and defocusing an image spreads the light from a genuine impact flash over a larger area. A lunar flash will be consequently defocused and will become a disk of comparable diameter. Defocusing will have no consequences on the images of spurious flashes, which will remain limited to 1 single pixel, thus allowing them to be distinguished from stars and eventual lunar flashes of impact origin. Another source of spurious flashes is due to glints off of satellites and space debris. They can be recognized by their motion during the acquired frames and for the periodicity of their light curves. In this article the detection of a space debris as more plausible source for the detected trailed flashes is described.

2. Instrument and Method

AVIs videos were recorded from Rome, observatory located at longitude 12.56076° E and latitude 41.94195° N, elevation 25 meters above the sea level. The coordinates of the observatory were determined using more than 100 map projections, including WGS84. The AVI were taken using a 13 cm f/6 TMB refractor and a Lumenera LU 075M camera set to 30 fps at a gamma of 1.0, gain of 14.00 and exposure times of 30 msec. The Lumenera camera, with an imaging array of 640 x 480 pixels, was used at prime focus with a filter IR blocking. The time was synchronized with US PA ntp-2.ece.cmu.edu. The synchronization for timing was checked daily using a GPS satellite signal with a difference of 0.002 sec. and a delay of 0.156 sec.

LTVT software package by Mosher and Bondo (2006) was used for lunar reference. The lunar quadrant for the acquisition of the video clips was the

GIF ANIMATION

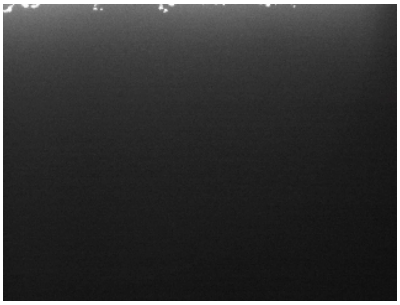

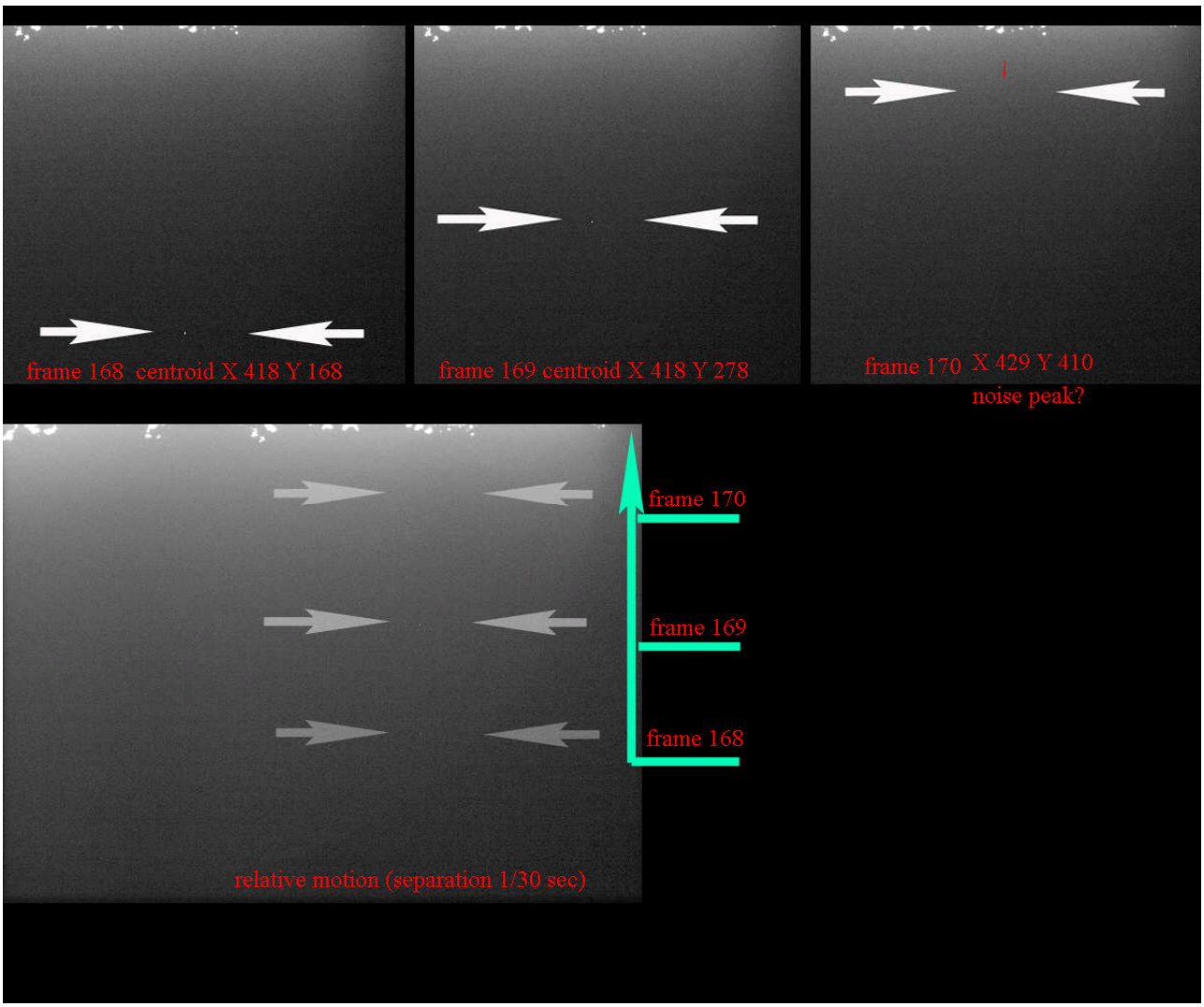

Figure 1 and preceding GIF animation: the track of the object across the moon

north-northwest region. Initially, the lunar terminator, correctly exposed, was positioned in a horizontal plane with north direction to the right and east at the top. Subsequently the images were slightly out of focus for the reason explained in section 1. The video clips were viewed visually in slow motion and also with a manual frame stepping using the software VirtualDub. Each clip was then analyzed using Lunarscan 1.3, a freeware program for lunar meteorite impact analysis written by Peter Gural. The identified flashes were extracted from the AVI film and saved as single frames in BMP format. An animated GIF in slow motion was then created using Photoshop Image Ready. A delay was assigned to each frame and a looping was specified so that the animation runs continuously.

3. Result and discussion

In the video VB19, taken on August 8 2008 a bright flash appeared trailed for three frames, in direction from west to east. It was detected in frame 168 at 19:05:06.2 UT. The first flash (2 pixel in size) is located at centroid X 418 Y 168 and in the next frame 169 (separation of 1/30 sec) is detectable at centroid X 418 Y 278, with a track across the Y axis. In the third frame 170, a faint flash is detectable at centroid X 429 Y 410, which could also be a random noise peak. An animation in slow motion shows with evidence the track (GIF animation and Fig 1). Standard orbital two-line elements (TLEs) of 10000 artificial objects (satellites and space debris) were examined. Simulation of their transit was performed using the software Orbitron by Stoff (2005) and the service offered by Calsky (Arnold Barmettler).

The generated map (Barmettler A. CalSky www.CalSky.com) were then compared with the location of the detected flash in the original AVI film. The location of the objects in transit across the lunar surface was determined superimposing the extracted single frame onto the lunar terminator correctly exposed before each observing session. Using the best TLEs it was determined that an object FENGYUN 1C DEB (1999-025-AHJ) passed very close to the flash location. FENGYUN 1C DEB (1999-025-AHJ) is a debris part of the intercepted Chinese satellite. The very large number of debris from Fengyun-1C extends from 200 km to 4000 km in altitude, with the highest concentration near the break up altitude of approximately 850 km. The difference from predicted and measured time was of 3 sec and a slight parallel shift of the predicted track can be expected (Figure 2 is the generated map showing the track of the space debris using two different TLEs). The direction of the track, from west to east, was the same of the track predicted by Calsky.

Furthermore, on almost the same track another debris FENGYUN 1C DEB (1999-025-UX) should have crossed the field but with a large difference in time of 2.5 minutes later.

Hence the debris (1999-025-AHJ) is a more plausible source for the detected trailed flashes.

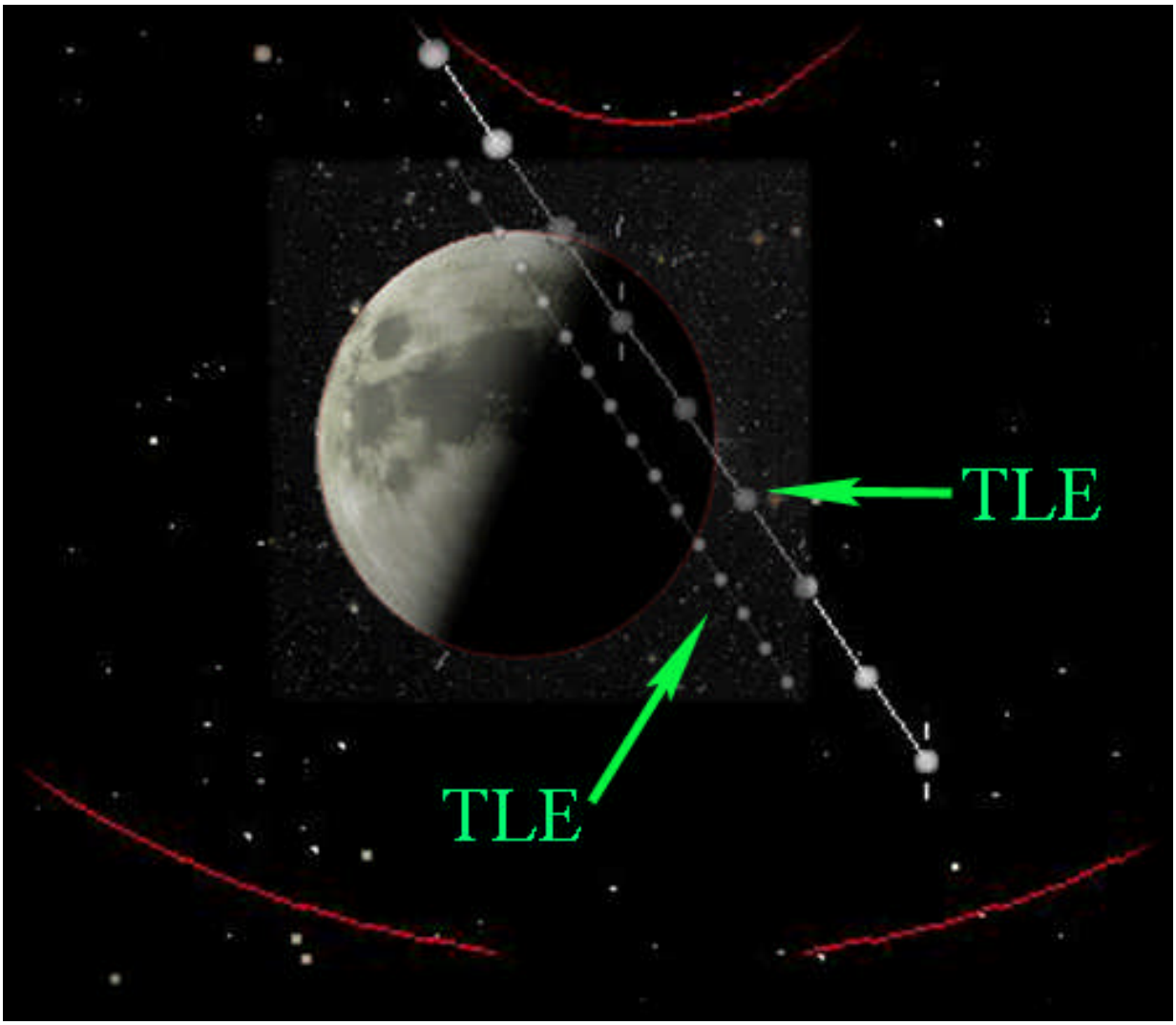

Figure 2: The track of the debris FENGYUN 1C DEB (1999-025-AHJ) computed using two different TLEs. The detected trailed flashes fall in this "window" in good agreement with two predictions (Arnold Barmettler, CalSky, www.CalSky.com).

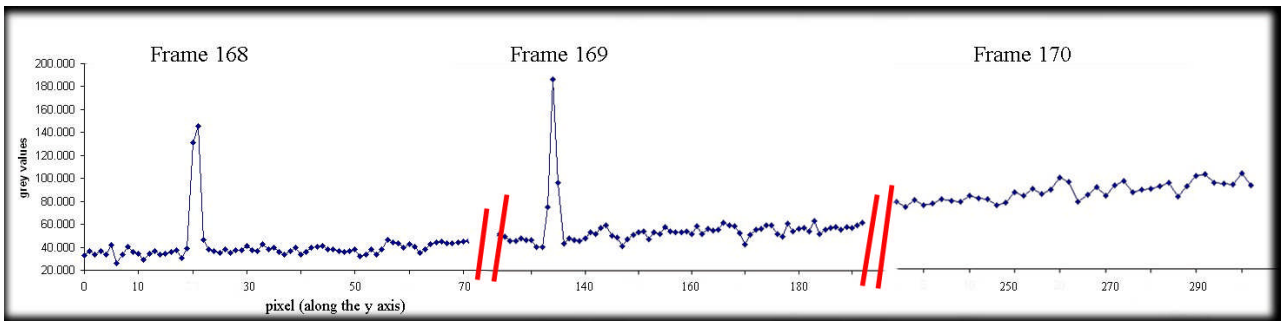

Figure 3: light curve derived from the photometric measures

The glint of this debris is strongly suggested for the periodicity of the light curve, shown in Fig. 3. According to the light source the space debris is possibly rotating which would explain the slightly changing brightness.

References

[1]Barmettler, A., "CalSky" www.CalSky.com

[2] Gural, P., Lunarscan. The program is available at **http://www.gvarros.com/lunarscan.zip.**

[3] Lena, R., and Evans, R., 2008. Observation for Lunar Meteoroid Impacts: Review of Current Techniques. Selenology Today. 9, pp.32-58.

[4] Lena, R., 2002. Manual for Lunar Impact Project (by ALS and GLR group) http://www.glrgroup.org/lunarimpact/manual.htm

[5] Mosher, J., Bondo, H., 2006. Lunar Terminator Visualization Tool (LTVT). http://inet.uni2.dk/ d120588/henrik/jim ltvt.html

[6] Stoff, S., 2005. Orbitron.

http://www.stoff.pl/

After the total eclipse of the moon last February, this year there was another eclipse of the Moon, also if a partial lunar eclipse. Indeed, the partial eclipse of the moon occurred on the evening of August 16-17 2008. Some images are shown in the following reports.

Patricio Dominguez lunar eclipse 08/16/2008 20:15 UT Madrid, Spain
Composite image (overlapping a 1/160s image and a 2" Image @ 100ASA).
Celestron C8, HEQ5, Celestron focal reducer and Canon Eos 20D

George Tarsoudis TSA-102N and Canon EoS 350D at prime focus

George Tarsoudis TSA-102N and Canon EoS 350D at prime focus

Partial lunar eclipse August 16 2008

19:57 UT

20:15 UT

21:02 UT

Raffaello Lena

TMB 13 cm refractor

Raffaello Lena Rome (Italy)

TMB 13 cm Refractor, Lumenera LU075M, ToUCam


22.15 U.T.
Iso 800 - 1/50 sec.
22.35 U.T.
Iso 800 - 1/2 sec.
22.53 U.T.
Iso 800 - 0,6 sec.
19.51 U.T.
Iso 800 - 1/160 sec.
22.59 U.T.
Iso 800 - 0,8 sec.
Eclisse parziale di Luna
16 agosto 2008
Canon 300D su MTO1000
Cristina e Fiorenzo Mazzotti
San Romualdo - Ravenna (Italy)

Brief Note: Upcoming LCROSS impact at lunar south pole

By Richard Evans
Geologic Lunar Research (GLR) Group

At a specific day and time still to be determined, most likely sometime between May and August 2009 (NASA appears to have moved an earlier tentative impact date ahead to the late spring/summer of 2009), NASA will launch the LCROSS probe on an Atlas rocket. For specific dates of launch and subsequent lunar impact of this probe, it is essential that you monitor the NASA LCROSS website. Its mission is to impact the lunar south polar region with the primary goal being to analyze the ejecta cloud for the presence of water vapor. Prior to this impact however, the upper stage of the Atlas rocket (Centaur) will first impact the moon while the LCROSS probe collects data. The most impressive impact will be by the LCROSS probe itself which reportedly weighs as much as a small truck and will provide an impact about ten times more energetic than the lunar Prospector probe and is predicted to be visible in 10 or 12 inch telescopes. Depending on the launch date, the specific impact site will be either Cabaeus, Faustini, or Shoemaker crater, but these are all in the same general area.

Specifics for imaging the impact are the same as for monitoring asteroid impacts on the moon and a discussion of equipment and procedures has been given in issue No. 9 of Selenology Today (Lena and Evans, 2008). Although attempts to record spectra of the impact might be attempted using a low resolution diffraction grating by Patton Hawkesley (100 line/mm) or Rainbow Optics (200 line/mm), it will not be possible for amateurs to obtain spectra of water vapor from the impact since this would require monitoring in the infrared from a high altitude site.

More information on the LCROSS mission can be obtained from the NASA website at: http://lcross.arc.nasa.gov/ and following additional links provided there. Those interested in observing or imaging the impact would do well to monitor the NASA LCROSS mission web site for more specific details on the dates, times and specific locations of the two impacts.